Is the presence of Sn 2+ a crucial factor for the generation of low thermal conductivity in tin-based sulfides?

Florentine Guiot, Carmelo Prestipino, Emmanuel Guilmeau, Paribesh Acharyya, Bernard Raveau, Susumu Fujii, Kaiyuan Yao, Thang Tran, Vincent Dorcet, Bernard Malaman, et al.

▶ To cite this version:

Florentine Guiot, Carmelo Prestipino, Emmanuel Guilmeau, Paribesh Acharyya, Bernard Raveau, et al.. Is the presence of Sn 2+ a crucial factor for the generation of low thermal conductivity in tin-based sulfides?. Inorganic Chemistry, 2024, 63 (32), pp.14889-14904. 10.1021/acs.inorgchem.4c01193 . hal-04686304

HAL Id: hal-04686304
https://hal.science/hal-04686304v1

Submitted on 4 Sep 2024

HAL is a multi-disciplinary open access archive for the deposit and dissemination of scientific research documents, whether they are published or not. The documents may come from teaching and research institutions in France or abroad, or from public or private research centers.

L'archive ouverte pluridisciplinaire **HAL**, est destinée au dépôt et à la diffusion de documents scientifiques de niveau recherche, publiés ou non, émanant des établissements d'enseignement et de recherche français ou étrangers, des laboratoires publics ou privés.

Is the presence of Sn^{2+} a crucial factor for the generation of low thermal conductivity in tin-based sulfides?

Florentine Guiot,[a] Carmelo Prestipino,[a,b*] Emmanuel Guilmeau*,[b] Paribesh Acharyya,[b]
Bernard Raveau,[b] Susumu Fujii,[c,d] Kaiyuan Yao,[c] Vincent Dorcet,[a] Bernard Malaman,[e]
Thierry Schweitzer,[e] Erik Elkaïm,[f] Masato Yoshiya,[c,d] Pierric Lemoine.[e,*]

[a] *Univ. Rennes, CNRS, ISCR-UMR 6226, F-35000 Rennes, France*
[b] *CRISMAT, CNRS, Normandie Univ, ENSICAEN, UNICAEN, 14000 Caen, France*
[c] *Division of Materials and Manufacturing Science, Graduate School of Engineering, Osaka University, Osaka 565-0871, Japan*
[d] *Nanostructures Research Laboratory, Japan Fine Ceramics Center, Nagoya 456-8587, Japan*
[e] *Institut Jean Lamour, UMR 7198, CNRS, Université de Lorraine, 54011 Nancy, France*
[f] *Synchrotron SOLEIL, L'orme des Merisiers, 91192 Gif-sur-Yvette, France*

* *Corresponding authors: pierric.lemoine@univ-lorraine.fr, Carmelo.prestipino@ensicaen.fr*

ABSTRACT

Comprehending the relationship between crystal structures and transport properties is crucial for developing materials with improved electrical and thermal properties for thermoelectric applications. In this article, we report on the complex crystal structure and physical properties of $Cr_2Sn_3S_7$, an n-type magnetic semiconductor with a low energy band gap and low thermal conductivity. Importantly, we demonstrate that the high level of structural complexity is related to the coexistence of two sublattices: a host lattice, $[Cr_4Sn_2S_{11}]^{2-}$, characterized by a mixed Sn^{4+}/Cr^{3+} occupancy of its cationic sites, and a guest lattice characterized by $[Sn_4S_3]^{2+}$ chains, containing only Sn^{2+} cations, closely related to those encountered in the orthorhombic SnS compound. By combining experiments, including X-ray diffraction, with *ab initio* calculations of electrons and phonons, we elucidated the origin of the low thermal conductivity in $Cr_2Sn_3S_7$. We demonstrate that the low dimensionality of the $[Sn_4S_3]^{2+}$ chains, which generates weak Sn···S interactions with the 3D host lattice, is induced by the lone pair stereochemical activity of Sn^{2+}. This lattice softening favors strong anisotropic vibrations at low frequencies, highlighting the primordial role played by Sn^{2+} cations in both crystal structure dimensionality and low thermal conductivity in tin-based sulfides.

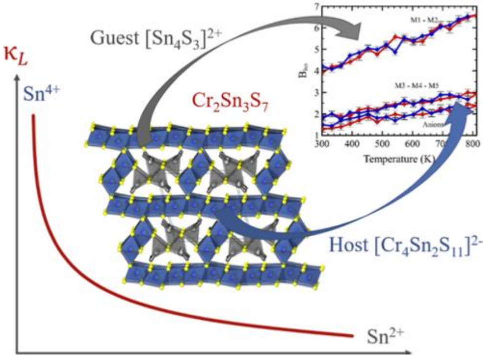

Introduction

Transition and post-transition metal (M) sulfides form a vast family of materials that have been extensively investigated for their optical, ionic, electrical, and thermal properties. These properties are crucial for various applications, including optoelectronic devices (Refs. 1, 2), catalysis and photocatalysis (Refs. 3), magnetism (Ref. 4), and energy-related applications such as solid-state batteries (Refs. 5–7), magnetocalorics (Ref. 8), solar cells (Refs. 9, 10), and thermoelectricity (Refs. 11–13). A significant aspect of research on thermoelectrics is identifying a material that can exhibit both high electrical conductivity and low thermal conductivity simultaneously (Ref. 14). The antagonist nature of these two properties means they cannot be easily optimized within the same metal-sulfur (M–S) lattice, leading to a compromise between the two effects.

This challenge is exemplified by the large family of thermoelectric (TE) mineral derivative copper sulfides (Ref. 15), such as tetrahedrite (Refs. 16–20), colusite (Refs. 11, 21–24), stannoidite (Refs. 25, 26), and mohite (Refs. 27, 28), whose electrical conductivity can generally be enhanced through adequate doping of the Cu–S framework based on the Cu(I)–Cu(II) mixed valence concept (Ref. 29). In addition to optimizing mineral derivative materials, the design of synthetic phases is another approach to developing attractive TE materials, particularly those made from nontoxic, eco-friendly, and earth-abundant elements (Ref. 30). This is exemplified by the copper-tin-sulfide system (CTS), which includes notable TE synthetic phases such as $Cu_4Sn_7S_{16}$ (Refs. 31, 32), $Cu_5Sn_2S_7$ (Refs. 33, 34), and $Cu_{22}Sn_{10}S_{32}$ (Refs. 35–37).

While there is ongoing debate about the conditions necessary to achieve low thermal conductivity without impacting carrier mobility, similar phenomena have been observed in non-copper-based TE sulfides. Notably, numerous studies on SnS are significant in this context. SnS exhibits a layered crystal structure with low symmetry and possesses a relatively large band gap of 1.05 eV at room temperature (RT) (Ref. 38). Despite the intrinsically low carrier concentration in wide band gap semiconductors, the high carrier mobility in SnS crystals mitigates the negative effects on electrical conductivity, allowing it to exhibit a relatively high anisotropic TE figure of merit, $ZT\ (= {S^2T}/{\rho\kappa})$, where S, ρ, κ, and T represent the Seebeck coefficient or thermopower, electrical resistivity, total thermal conductivity, and operating absolute temperature, respectively). This anisotropy in the crystal is primarily observed in the electrical conductivities, with significantly higher values along the b and c axes (~20 S cm^{-1}) compared to the a axis (~4 S cm^{-1}) (Ref. 39). The Seebeck coefficient demonstrates isotropic behavior, and the c direction exhibits a high power factor (~700 μW $m^{-1}\cdot K^{-2}$ at 823 K) (Ref. 39). Combined with low thermal conductivity (~0.78 $W\cdot m^{-1}\cdot K^{-1}$ at 873 K), this results in a high ZT value close to 1 at 873 K along the c direction in a SnS single crystal (Ref. 39). In contrast, polycrystalline samples prepared using conventional ceramic methods fail to achieve such high ZTs, yielding modest power factors (124.8 μW $m^{-1}\cdot K^{-2}$ at 823 K) (Ref. 40) and ZTs not exceeding 0.21 at 877 K (Refs. 40, 41).

To achieve high TE performance in polycrystalline SnS samples, several innovative approaches have been employed. For instance, doubling the thermoelectric performance (ZT = 0.41 at 848 K) was accomplished by halving the thermal conductivity (0.29 $W\cdot m^{-1}\cdot K^{-1}$ at 848 K) through a chemical precipitation synthesis method (Ref. 42). Additionally, nonstoichiometric Sn_xS samples synthesized via a microwave hydrothermal method exhibit notably higher ZT values, reaching 0.76 at 523 K (x = 0.13) (Ref. 43). This enhancement is attributed to the increased power factor (830.6 μW $m^{-1}\cdot K^{-2}$ at 523 K) without compromising the total thermal conductivity (0.57 $W\cdot m^{-1}\cdot K^{-1}$) (Ref. 43). Another alternative approach to enhancing the ZT of SnS material involves increasing charge carrier concentration through doping, such as $Sn_{1-x}A_xS$ (with A = Ag, Na, Tl, Li, and Pb) (Refs. 41, 44–47) and $SnS_{1-x}B_x$ (with B = Br, Cl, and Se) (Refs. 48–51). Among these dopants, Ag and Li (which are p-type dopants that increase carrier concentration) have been particularly effective, allowing for ZT values of 0.66 at 848 K (x = 0.02) (Ref. 44) and 1.1 at 877 K (x = 0.005) (Ref. 41), respectively. A consistent feature across all synthesis approaches is the remarkably low total thermal conductivity of SnS samples, which does not exceed 1 $W \cdot m^{-1} \cdot K^{-1}$, resulting from strong lattice anharmonicity (Ref. 52). From this discussion, it is evident that extensive research has been conducted to optimize the TE performance of polycrystalline SnS. However, despite the considerable number of scientific publications on this promising material, the role of the lone electron pair of Sn^{2+} in optimizing these antagonistic properties is not yet fully understood.

Recently, we proposed a strategy to simultaneously optimize electrical and thermal conductivities within the same crystal structure of copper-based sulfides. This approach involves frameworks characterized by the coexistence of two different and independent Cu–S sublattices: one devoted to high electrical conductivity (the tetrahedral "CuS_4" sublattice) and the other to low thermal conductivity (the threefold "CuS_3" sublattice) (Ref. 53). We believe that this strategy of employing two sublattice systems within the same compound could also be a promising direction for developing high-performance non-copper-based systems. Consequently, we have embarked on research into new synthetic Sn^{2+}-rich sulfides containing environmentally friendly elements, with frameworks composed of two different M–S sublattices.

In this report, we present the sulfide $Cr_2Sn_3S_7$, which, like SnS, exhibits a low lattice thermal conductivity (κL) of 0.77 $W \cdot m^{-1} \cdot K^{-1}$ at 300 K. We highlight that the complex crystal structure of this sulfide is composed of two sublattices: a tunnel host framework $[(Cr^{3+})_4(Sn^{4+})_2S_{11}]^{2-}$, which is filled by guest chains $[(Sn^{2+})_4S_3]^{2+}$. Remarkably, the geometry of the guest $[(Sn^{2+})_4S_3]^{2+}$ chains, which is closely related to the SnS structure, plays a key role in the low κL of this material due to the low vibration frequencies of the Sn^{2+} cations. Additionally, we show that the random cationic distribution within the host framework $[(Cr^{3+})_4(Sn^{4+})_2S_{11}]^{2-}$

contributes, albeit to a lesser extent, to the low κL of $Cr_2Sn_3S_7$. However, this distribution also results in lower electrical conductivity and power factor.

Thus, this study paves the way for the exploration and investigation of transition metal sulfides with complex structures composed of different and independent sublattices.

Experimental section

$Cr_2Sn_3S_7$ was synthesized using a ceramic method adapted from that reported by Jobic et al. for preparing the selenide phase $Cr_2Sn_3Se_7$ (Ref. 54). Chromium powder (~60 mesh, Fluka AG, 99.9%), tin powder (~100 mesh, Strem Chemicals, 99.8%), and sulfur pieces (Strem Chemicals, 99.999%) were mixed in a molar ratio of 2:3:7 to achieve a total mass of 5 g. The mixture was ground together and then sealed in an evacuated silica tube. It underwent heat treatment for 4 days at 1098 K with a heating rate of 1 K min^{-1}. The laboratory X-ray powder diffraction (XRPD) pattern of the as-prepared products revealed minor impurities (Cr_2S_3 and Cr_2SnS_4).

The synthesized powders were densified using spark plasma sintering (SPS, FCT HP D 10) for 60 minutes at 1023 K under a uniaxial pressure of 64 MPa. The heating and cooling rates were 50 K min^{-1} and 20 K min^{-1}, respectively. The final pellet had dimensions of approximately 8 mm in thickness and 10 mm in diameter, with a density of ~97% of the theoretical value. Post-sintering, the quantity of impurities was significantly reduced, and no unusual hazards were noted.

Single crystals suitable for single-crystal X-ray diffraction (SCXRD) were grown under similar conditions to those used for powder samples, with the exception of an extended dwell time of 6 days at 1098 K. Several pinacoid-shaped crystals, averaging ~50 × 50 × 10 μm^3, were obtained and analyzed. SCXRD was performed at 293 K using a Rigaku XtaLAB Synergy diffractometer, equipped with a microfocus sealed X-ray tube (Mo−Kα X-ray wavelength, λ = 0.71073 Å) and an Eiger 1 M hybrid pixel array detector.

Purity and structural characterization of powder samples were conducted using XRPD in θ−2θ Bragg−Brentano geometry with a D8 ADVANCE diffractometer. This setup included a Cu Kα radiation source, a Ge(111) monochromator, and a silicon strip LynxEye detector. Additional synchrotron XRPD data were collected on a 2-circle diffractometer in Debye−Scherrer geometry at the CRISTAL beamline of the SOLEIL synchrotron (Saint-Aubin, France), with a wavelength $\lambda = 0.58143$ Å. The beamline uses an undulator source monochromated by a Si(111) double-crystal monochromator. To avoid absorption correction, the powder sample was mixed with fumed silica in a 50:50 weight ratio and placed in a borosilicate capillary (Ø = 0.5 mm).

Diffraction pattern analysis was performed using Rietveld profile refinement with FullProf and WinPLOTR software packages (Refs. 55, 56). The diffraction peaks were modeled with a Thompson−Cox−Hastings pseudo-Voigt profile function (Ref. 57). Structural parameters, zero-point shift, and asymmetry parameters were systematically refined, and background contribution was modeled with a Chebyshev polynomial function (Ref. 58). The March−Dollase model (Ref. 59) was used to quantify and correct the degree of preferred orientation in the XRPD pattern.

Structural characterization of the powder sample at high temperature was performed using XRPD in Debye−Scherrer geometry. For this, a quartz capillary with a 0.3 mm diameter, sealed under vacuum, was used, along with a D8 ADVANCE diffractometer equipped with a Mo Kα radiation source (selected by a focusing multilayer mirror) and a LynxEye HE detector. Data were collected in the angular range $4 \leq 2\theta/° \leq 35$ with a step size of 0.0120° at every 30 K increment from 300 to 810 K.

The low symmetry of $Cr_2Sn_3S_7$, combined with the low resolution and ordinary statistics associated with laboratory in situ experiments using a Mo source, makes Rietveld refinement of individual patterns less reliable and precise for the total experiment. To achieve more reliable results, the data were analyzed using a parametric approach or surface plot within the Topas academic software (Ref. 60).

In this approach, patterns were considered collectively, and the parameters defining both the phase and instrumental contributions to the signal were constrained as a function of temperature. Four typical constraints were applied: (i) The zero-displacement error and atomic site coordinates were assumed to be common for all patterns (Table S1), meaning they were independent of temperature. (ii) The unit cell parameters were constrained to an Einstein-like model.

$$\mathrm{a(T)} = a_0 + \frac{c_1\theta_\mathrm{E}}{e^{(\theta_\mathrm{E}/T)} - 1}$$

with a_0, c_1, and θ_E as refinable parameters; (iii) the angle β was constrained to follow a polynomial function of degree 3 with respect to temperature; and (iv) isotropic thermal parameters (B_{iso}) were restrained to three variable groups (M1 and M2 sites; M3, M4, and M5 sites; S sites) without additional constraints. All other parameters were refined independently. Note that despite employing this constrained refinement procedure, the accordance of the fitted curves with the experimental data remains high (Figure S1).

Bulk polycrystalline samples were analyzed by EDX (energy dispersive X-rays) equipment implemented on a JEOL JSM-7100F scanning electron microscope. These analyses provide a chemical formula of $Cr_{1.98(1)}Sn_{3.30(1)}S_7$ (Cr: 16.1% ± 0.3; Sn: 26.9% ± 0.2; S: 57.0% ± 0.2) which is in satisfactory agreement with the expected composition (*i.e.* $Cr_2Sn_3S_7$), and the experimental compositions determined by single-crystal diffraction (*i.e.* $Cr_{1.89(4)}Sn_{3.01(3)}S_7$) and synchrotron XRPD (*i.e.* $Cr_{1.99(2)}Sn_{2.93(2)}S_7$). Considering the intrinsic experimental errors, variability of the different synthesis batches, and for the sake of simplicity, this new ternary phase will be mentioned in the rest of the article using its nominal composition, *i.e.* $Cr_2Sn_3S_7$.

223 Electron diffraction (ED) studies were conducted on powder samples using a JEOL JEM 2100 LaB6 microscope operated at 200 kV, equipped with a GATAN ORIUS 200D CCD camera. A transmission electron microscopy (TEM) specimen was prepared by grinding the material in an agate mortar with ethanol and then depositing a drop of the resulting suspension onto a Cu carbon grid. The diffraction patterns were analyzed using TEMpcPlot, a Python code designed for indexing TEM image sequences.(Ref. 61) Magnetic measurements were performed on polycrystalline sample after SPS using a SQUID magnetometer (MPMS XL5, Quantum Design). For dc measurements, the sample was first cooled down in zero field up to 1.8 K, the field was applied at 0.1 T and the measurements taken with increasing the temperature up to 300 K (ZFC curves). Then the samples were cooled down again at constant field and a new set of measurements done with increasing the temperature (FC curves). At high temperature paramagnetic regime, the inverse magnetic susceptibility χ was fitted using the Curie-Weiss law:

$$\frac{1}{\chi(T)} = \frac{(T - \theta_p)}{C}$$

With *C* the curie constant, *T* the temperature and θ_p the paramagnetic Curie temperature. The effective moment of the magnetic atom μ_{eff} is deduced from the curie constant by the relation:

$$\mu_{eff} = \sqrt{8C}\ \mu_{\mathrm{B}}/\mathrm{at}$$

^{119}Sn Mössbauer spectra of powder sample were measured at $T = 300$, 120, 50, 40, 30, and 4 K in transmission geometry with a spectrometer operating in the conventional constant-acceleration mode. Polycrystalline absorber with a natural abundance of ^{119}Sn isotope and a real density of ~15 mg cm^{-2} was used. The Ba^{119}SnO$_3$ source with a nominal strength of 10 mCi source was kept at room temperature (RT). A palladium foil of 0.5 mm thickness was used as a critical absorber for tin X-rays. Velocity calibration was done at RT using a 12 μm-thick α-

Fe foil. Mössbauer spectra were fitted with a least-squares method program assuming Lorentzian peaks. ^{119}Sn isomer shifts (IS) are referred to $BaSnO_3$ at RT.

The optical properties of the powder sample were investigated using a PerkinElmer Lambda-8 UV−vis spectrophotometer with a reflectance spectroscopy accessory to collect diffuse-reflectance UV−vis spectra. The sample was ground for a few minutes and loaded into a custom sample holder, and the spectra were collected at an interval of 4 nm at a scan rate of 120 nm min^{-1} with a slit size of 3 nm.

The electrical resistivity (ρ) and Seebeck coefficient (S) were measured simultaneously from 3 × 3 × 8 mm^3 ingots, from 300 to 700 K using an ULVAC-ZEM3 instrument under partial helium pressure. Laser flash analysis performed by A NETZSCH LFA-457 apparatus was used for measuring the thermal diffusivity under argon flow from 6 × 6 × 2 mm^3 pellet. Thermal conductivity κ (W m^{-1} K^{-1}) was calculated from the product of thermal diffusivity (D), density (d) and heat capacity (Cp):

$$\kappa = D \times C_p \times d \quad with: C_p = \frac{3nN_a k_B}{M}$$

C_p has been estimated with the Dulong-Petit approximation (Ref. 62), where n is the number of atoms in the chemical formula, N_a Avogadro number (6.022×10^{23} mol^{-1}), and Boltzmann constant: k_B (1.381×10^{-23} kg m^2 s^{-2} K^{-1}) and molar weight M (kg mol^{-1}). The estimated measurement uncertainties are 6% for the Seebeck coefficient, 8% for the electrical resistivity, 11% for the thermal conductivity, and 16% for the final figure of merit, ZT. (Ref. 63).

Ab initio calculations were performed for the structure optimization and evaluation of the physical properties of $Cr_2Sn_3S_7$. The plane-wave basis projector augmented wave (PAW) method (Ref. 64) was used as implemented in the Vienna Ab initio Simulation Package (VASP) (Refs. 65, 66). We employed the generalized gradient approximation (GGA) of PBEsol proposed by Perdew et al. (Ref. 67) for the exchange–correlation functional, after finding better reproducibility of structures compared with the PBE functional (Ref. 68). The Hubbard model for the GGA + U scheme was also employed to consider localization of 3d orbitals of Cr, with a U value of 3.5 eV (Ref. 69). A plane-wave energy cutoff was set to 380 eV. The first Brillouin zone was sampled with Monkhorst–Pack k-point grids of 3 × 7 × 3 for the ordered models and 3 × 3 × 3 for the semiordered model, respectively (see below for the details of the models). The criteria of total energy convergence and residual forces acting on atoms were set to 1.0×10^{-6} eV/cell and 8.0×10^{-3} eV/Å, respectively. The PAW pseudopotentials for Cr, Sn, and S used in this study contain the valence electrons of $3p^6\ 3d^5\ 4s^1$, $4d^{10}\ 5s^2\ 5p^2$, and $3s^2\ 3p^4$, respectively, with the rest core electrons frozen. High-spin states of cations were assumed in the beginning of all of the electronic structure calculations after finding from preliminary calculations with various initial spin states that Cr^{3+} and Sn^{2+}/Sn^{4+} ions arrive at high-spin and low-spin states, respectively, independent of the initial spin state.

We considered four structure models of $Cr_2Sn_3S_7$ with the ordered and semiordered cationic arrangements. For the three ordered models, we assumed that two of the three cation sites (M3, M4, and M5) were occupied by Cr atoms, and the other sites, including M1 and M2 sites, were occupied by Sn atoms (see the section of crystal structure analyses for the details of cationic sites and models in Supporting Information). For the semiordered model, we created a 1 × 3 × 1 supercell to represent partial occupancies of the cations. The partial occupancies of Sn (Cr) were approximated to 1.0 (0.0) for M1 and M2 sites and 1/3 (2/3) for M3, M4, and M5 sites, to maintain the nominal composition in each supercell. For the random distributions of the cations at M3, M4, and M5 sites in the semiordered model, special quasi-random structures (SQSs) (Ref. 70) were used as the best representation of the completely random structure within a given model sizes in general were generated using the ***corrdump*** and ***mcsqs*** codes (Ref. 71). The lattice parameters of the optimized structure are a=11.157 Å, b=3.6569 Å, c=12.125 Å, and β=105.46° for the semiordered model, consistent with experimental results.

The electronic band structures of a semiordered and three ordered $Cr_2Sn_3S_7$ models were calculated using the reciprocal path generated by the method reported by Hinuma et al. (Ref. 72). The electronic density of states (DOS) was calculated using finer Γ-centered k-point grids of 7×15×77 \times 15 \times 77×15×7 for the ordered model and 7×7×77 \times 7 \times 77×7×7 for the semiordered model, respectively. The phonon DOS and band structures of the ordered and semiordered $Cr_2Sn_3S_7$were calculated using the Phonopy code (Refs. 73–75). Atomic displacements of 0.01 Å were given to each symmetrically nonequivalent atom to calculate the forces acting on atoms and derive the second-order force constant tensors of second rank. For the ordered models, unit cells were repeated three times along the b axis to construct supercells to minimize the self-interactions between the displaced atoms beyond the periodic boundaries. Nonanalytical term correction (Ref. 76) was applied to all the models, with Born effective charges and dielectric constants calculated by density functional perturbation theory (Refs. 77, 78) implemented in the VASP code. Pairwise scalarized interatomic force constants were calculated according to the preceding study (Ref. 79). Thermal displacement ellipsoids were calculated within the harmonic approximation from 0 to 2000 K in order to comprehend anisotropic atomic vibrations, especially of the cations. Mode Grüneisen parameters were calculated within the quasi-harmonic approximation using the volumes under pressures of ±1 GPa.

.

Results

Crystal structure analyses

Laboratory X-ray powder diffraction (XRPD) analysis reveals that the $Cr_2Sn_3S_7$ powder sample prepared by sealed tube synthesis is mainly constituted of a phase crystallizing in a monoclinic space group $P2_1/m$ with unit cell parameters a = 11.268(1) Å, b = 3.648(1) Å, c = 12.209(1) Å, and β = 105.42(1)° (**Figure S1**). The electron diffraction from transmission electron microscopy study also revealed the monoclinic phase of $Cr_2Sn_3S_7$ with a lattice parameter of a = 11.5 Å, b = 3.7 Å, c = 12.5 Å and β = 105°, **Figure S2**). This is in line with a previous report by Corps (Ref. 80) and crystal data on related $In_2Sn_3S_7$ and $Cr_2Sn_3Se_7$ phases (Refs. 54, 81, 82). Considering the smaller ionic radius of chromium compared to indium on one hand, and the smaller ionic radius of sulfur compared to selenium on the other hand, it is reasonable to conclude that the primary phase identified by XRPD and TEM corresponds to the sulfide $Cr_2Sn_3S_7$. This phase likely crystallizes either in the semi-ordered $Cr_2Sn_3Se_7$-type structure or in the supposed ordered $In_2Sn_3S_7$-type structure.(Ref 81,82)This assumption is supported by the chemical formula of $Cr_{1.98(1)}Sn_{3.30(1)}S_7$ determined by EDX analyses. However, attempts to confirm, from Rietveld refinement, the structural model of $Cr_2Sn_3S_7$ was unsuccessful, mainly due to large uncertainties due to a very strong preferential orientation of the crystallites along the [100] direction (**Figure S1**). This preferential orientation is confirmed by transmission electron microscopy showing that the main phase is composed of grains with a platelet crystal habit (**Figure S2**) similar to the one reported for $In_2Sn_3S_7$. (Ref 81) In addition to the diffraction peaks arising from the monoclinic phase, few spurious low-intensity peaks ascribed to the Cr_2SnS_4 (Ref 83,84) and Cr_2S_3 (Ref 85) phases are also detected on the XRPD pattern. Note that XRPD analysis of the sample after SPS shows that the Cr_2S_3 phase is no longer present while traces of Cr_2SnS_4 are still present (**Figure S3**), indicates that SPS improves the sample purity.

In order to confirm the structural model of the main phase, a platelet shape single-crystal has been extracted from the powder sample and analyzed by X-ray diffraction. The results confirm the monoclinic lattice (a = 11.273(4) Å, b = 3.643(2) Å, c = 12.220(5) Å and β = 105.358(10)°, **Table S1**) with space group $P2_1/m$, the chemical composition of $Cr_2Sn_3S_7$ and the similarity of the crystal structure with that of $Cr_2Sn_3Se_7$ (**Table S2 and S3**). Indeed, in $Cr_2Sn_3S_7$, sulfur and metallic atoms are located on seven and five different 2e sites (x, ¼, z). As reported for

$Cr_2Sn_3Se_7$ (Ref 54) the agreement factor for single-crystal X-ray diffraction (SCXRD) is significantly improved when there is a mixed occupancy of Cr and Sn atoms in the octahedral coordinated sites (i.e., M3, M4, and M5), while M1 and M2 sites are occupied solely by Sn atoms. Moreover, the Fourier difference map also indicates a weak electron deficiency on the M2 site and possibly on the M1 site, which is eventually attributed to vacancies after considering crystal chemistry aspects (i.e., site symmetry and coordination of cations). Refinement of the site occupation factors reveals that, in $Cr_2Sn_3S_7$, the M1 and M2 sites are almost entirely occupied by Sn, whereas the M3, M4, and M5 sites are occupied approximately two-thirds by Cr and one-third by Sn (Table S3). This leads to the refined chemical composition $Cr_{1.89(4)}Sn_{3.01(3)}S_7$, in good agreement with the nominal composition.

In order to obtain a representative analysis of the entire sample, high-resolution synchrotron X-rays powder diffraction was performed at the CRISTAL beamline at Synchrotron SOLEIL in Debye-Scherrer configuration. The data collected in Debye-Scherrer geometry do not exhibit any sign of preferential orientation and have been analyzed by Rietveld refinement (**Figure 1** and **Figure S5**). These data confirm the structural model of $Cr_2Sn_3S_7$ (**Table 1**) determined from single-crystal XRD, the presence of traces of Cr_2SnS_4, and a refined chemical composition of $Cr_{1.98(2)}Sn_{2.93(2)}S_7$ in excellent agreement with the nominal composition.

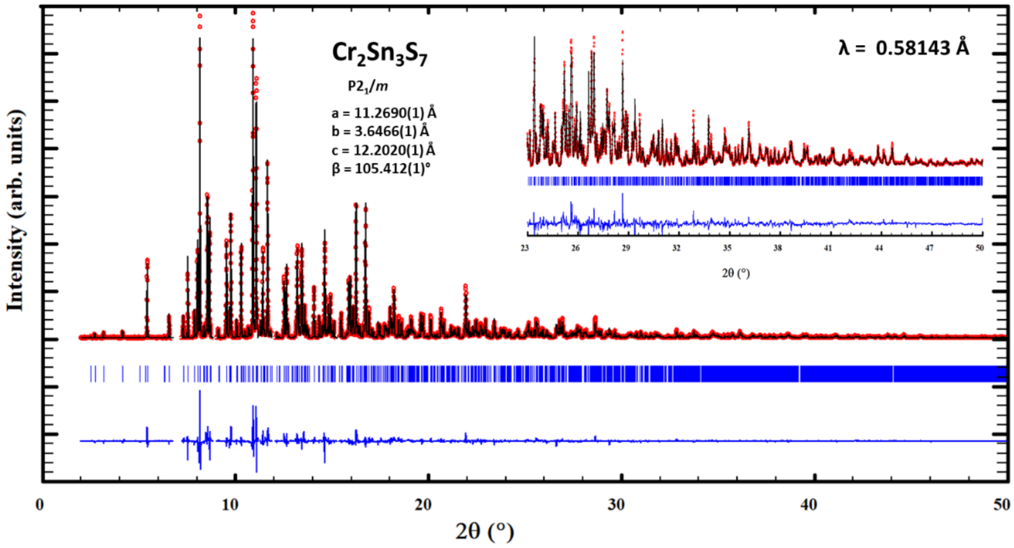

Figure 1: Rietveld refinement of the high-resolution synchrotron XRPD pattern recorded at RT (λ = 0.58143 Å) on the $Cr_2Sn_3S_7$ sealed tube synthesis sample.

Table 1: Crystallographic data of $Cr_2Sn_3S_7$ from the Rietveld refinement of the synchrotron X-ray powder diffraction data recorded at RT.

$P2_1/m$, a = 11.2690(1) Å, b = 3.6466(1) Å, c = 12.2020(1) Å, β = 105.412(1)°							
Label	Element	Site	x	y	z	SOF	U_{iso}/U_{equiv} (Å^2)
S1	S	2e	0.9009(3)	¼	0.8906(3)	1.00	0.0122(20)
S2	S	2e	0.3958(3)	¼	0.1835(3)	1.00	0.0104(19)
S3	S	2e	0.6108(3)	¼	0.5842(3)	1.00	0.0120(20)
S4	S	2e	0.3499(3)	¼	0.6720(3)	1.00	0.017(2)
S5	S	2e	0.6271(2)	¼	0.0627(3)	1.00	0.0138(19)
S6	S	2e	0.9080(3)	¼	0.2583(3)	1.00	0.015(2)
S7	S	2e	0.8872(3)	¼	0.5276(3)	1.00	0.0097(19)
M1	Sn	2e	0.16316(9)	¼	0.28299(10)	0.981(3)	0.0239(7)
M2	Sn	2e	0.15667(10)	¼	0.95893(11)	0.935(1)	0.0364(9)
M3	Sn/Cr	2e	0.11310(11)	¼	0.61140(12)	0.37(1)/0.63(1)	0.0066(9)
M4	Sn/Cr	2e	0.48565(12)	¼	0.87343(13)	0.29(1)/0.70(1)	0.0080(8)
M5	Sn/Cr	2e	0.52536(12)	¼	0.38090(12)	0.35(1)/0.65(1)	0.0075(8)

The crystal structure of $Cr_2Sn_3S_7$, shown in **Figure 2**, can be described as a tunnel structure whose $[Cr_4Sn_2S_{11}]^{2-}$ host framework forms four-sided tunnels running along the *b*-

axis, where guest $[Sn_4S_3]^{2+}$ chains are located. The host framework $[Cr_4Sn_2S_{11}]^{2-}$ is built up of edge and corner-sharing CrS_6 and SnS_6 octahedra, where Cr^{3+} and Sn^{4+} cations are randomly distributed (M3, M4 and M5 sites, in blue in **Figure 2**). The octahedral host framework $[Cr_4Sn_2S_{11}]^{2-}$ is composed of CdI_2-type puckered layers (M4, M5 sites), similar to those observed in misfit sulfides. However, two successive layers along the *c*-axis are linked one to another through two-octahedra-thick [010] rock salt ribbons of edge-sharing octahedra (M3 site) by sharing the apices of their octahedra, leading to tunnels oriented along the *b*-axis. The guest $[Sn_4S_3]^{2+}$ chains hosted in the tunnels are formed by units of Sn^{2+} cations (M1, M2 site, in grey in **Figure 2a-b**) linked to three S^{2-} anions (M1-S1, M1-S6 and M2-S1), showing strong similarity with α-SnS (herzenbergite, GeS structure type (Ref 86)). The environment of these cations, completed by the lone pair electrons (L) of Sn^{2+}, can be viewed as pseudo-tetrahedral SnS_3L and is responsible for ~~of~~ the weak bonding of the guest $[Sn_4S_3]^{2+}$ chains to the $[Cr_4Sn_2S_{11}]^{2-}$- host framework (see below).

Note that the crystal structure of $Cr_2Sn_3S_7$ is isotypic to the monoclinic form of $Cr_2Sn_3Se_7$, (Ref 54) but shows also some similarities with the orthorhombic form. (Ref 87) The latter also exhibits a tunnel structure but with a different host framework composed of six edge-sharing octahedra ribbons alternatively stacked within two different orientations, and with guest unit composed of ribbons of Sn atoms linked to three S atoms located in the tunnels (**Figure S6**), equivalent to those encountered in $Cr_2Sn_3S_7$.

All cationic sites forming the $[Cr_4Sn_2S_{11}]^{2-}$ host framework (M3, M4 and M5) exhibit a slightly distorted octahedral coordination characterized by average M-S distances of 2.496 Å, 2.470 Å and 2.480 Å, respectively (**Table S6**). Note that the slightly longer M-S4 distances, compared to the other ones constituting MS_6 octahedra, is related to the four-fold coordination of S4 atoms (S2, S3, S5, S6, and S7 atoms having a three-fold coordination) since this sulfur atom is shared between one octahedral slab and one octahedral ribbon. Bond valence sum (BVS) calculation[82]

(**Table S6**) shows that all octahedral sites exhibit the valences Sn^{4+} and Cr^{3+} exclusively, as shown for example for the M3 site (**Table S4**), whose the expected BVS value are close to the experimental one of 3.23 (1.689 + 1.540), while the expected value with Sn^{2+} is 2.63 and the experimental one is 3.37 (= 1.831 + 1.540). Hence, BVS calculation allows to exclude the presence of Sn^{2+} in the octahedral sites (*i.e.* M3, M4 and M5). Thus, based on these crystal chemistry investigations, octahedral MS_6 sites (*i.e.* M3, M4 and M5) are statistically occupied by both Cr^{3+} and Sn^{4+} cations, while the two other sites (*i.e.* M1 and M2) are fully (or almost fully) occupied by Sn^{2+} cations. This leads to a formal oxidation states formula, of $(Cr^{3+})_{1.98(2)}(Sn^{2+})_{1.92(2)}(Sn^{4+})_{1.01(2)}(S^{2-})_7$ in excellent agreement with the expected one, $(Cr^{3+})_2(Sn^{2+})_2(Sn^{4+})_1(S^{2-})_7$.

The guest ribbons are composed of cationic sites M1 and M2, almost fully occupied by Sn^{2+}, according to the formulation $[Sn_4S_3]^{2+}$. BVS calculation (Ref 88) (**Table S6**) clearly shows the presence of Sn^{2+}exclusively for both sites. If all interacting Sulphur atoms are taken into account, Sn^{2+} cations are located in strongly distorted bi-capped trigonal prismatic environments (CN = 8). This local structure has already been observed in the $SnS-SnS_2-In_2S_3$ system (Refs. 80–82, 89–90), where the two valences, Sn^{2+}/Sn^{4+}, can also coexist, as seen, for instance, in $In_2Sn_3S_7$ (Refs. 81, 82) and $In_6Sn_8S_{19}$ (Ref. 89). The polyhedra around Sn^{2+} are composed of two sets of Sn−S distances: three relatively short distances (M1: 2 Sn1−S1 and 1 Sn1−S6, and M2: 3 Sn2−S1) ranging from 2.742 to 2.810 Å (similar to the herzenbergite, Ref. 86) and five much longer distances (M1: 1 Sn1−S2, 2 Sn1−S3, and 2 Sn1−S7, and M2: 1 Sn2−S2, 2 Sn2−S5, and 2 Sn2−S6) ranging from 3.110 to 3.293 Å (Table S6). Importantly, from a vibrational perspective in these chains, the long-distance interactions are of secondary importance compared to the three shorter Sn−S bonds. In this context, the coordination shell of Sn^{2+} is better described as a SnS_3L tetrahedron with the $5s^2$ lone electron pair (L) of Sn^{2+} (Figure 2).

Consequently, the guest ribbons $[Sn_4S_3]^{2+}$ can be described as chains of corner-sharing SnS_3L tetrahedrons running along *b*. The nature of the chemical bonding within these chains and between the chains and the host framework $[Cr_4Sn_2S_{11}]^{2-}$ is expected to play a crucial role in the thermal conductivity of this sulfide. It is worth underlining that the $[Sn_4S_3]^{2+}$chains are anchored to the walls of the tunnels through the S6 atom, but that their S1, Sn1 (M1), Sn2 (M2) atoms can vibrate rather freely due to the fact that they exhibit much weaker Sn---S interactions with the host framework. This is attested by the significantly longer Sn---S distances (ranging from 3.11 to 3.29 Å) between the chains and the host lattice, compared to the strong iono-covalent Sn-S bonds within the chains (2.74 to 2.81 Å). As discussed further, this point suggests a significant anisotropy of the thermal conductivity which is expected to be higher along *b* due to the stronger Sn-S bonds than in the perpendicular directions where the Sn---S interactions are much weaker.

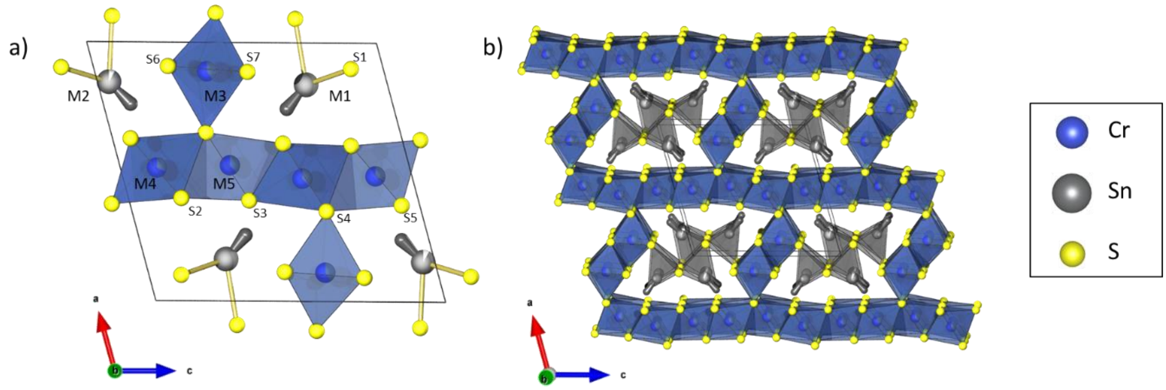

Figure 2 : Projections of the crystal structure of $Cr_2Sn_3S_7$ along the *b* axis highlighting: (a) the three-fold sulfur coordination of M1 and M2 sites occupied only by Sn^{2+} cations and completed by its lone pair (L) electrons, and the octahedral M3, M4 and M5 sites occupied by Cr^{3+} and Sn^{4+} cations in an almost 2/1 ratio; (b) the host edge and corner-sharing octahedron $[Cr_4Sn_2S_{11}]^{2-}$ framework (blue colored) and its guest $[Sn_4S_3]^{2+}$ - ribbons (grey colored).

High temperature PXRD

To evaluate the structural stability and estimate the thermal expansion for the typical temperature range of thermoelectric (TE) generators based on sulfide materials, a $Cr_2Sn_3S_7$ sample was investigated by in situ X-ray powder diffraction (XRPD) at high temperatures. The XRPD patterns collected during warming to 800 K and subsequent cooling are shown in Figure 3. These data suggest that, under vacuum, the $Cr_2Sn_3S_7$ phase demonstrates excellent stability and reversibility. This is evidenced by (i) the sample remaining in a single phase throughout the experiment (Figure S1) and (ii) the diffraction patterns recorded at room temperature before and after high-temperature exposure being very similar. Therefore, any variation in peak positions can be attributed solely to thermal expansion and contraction.

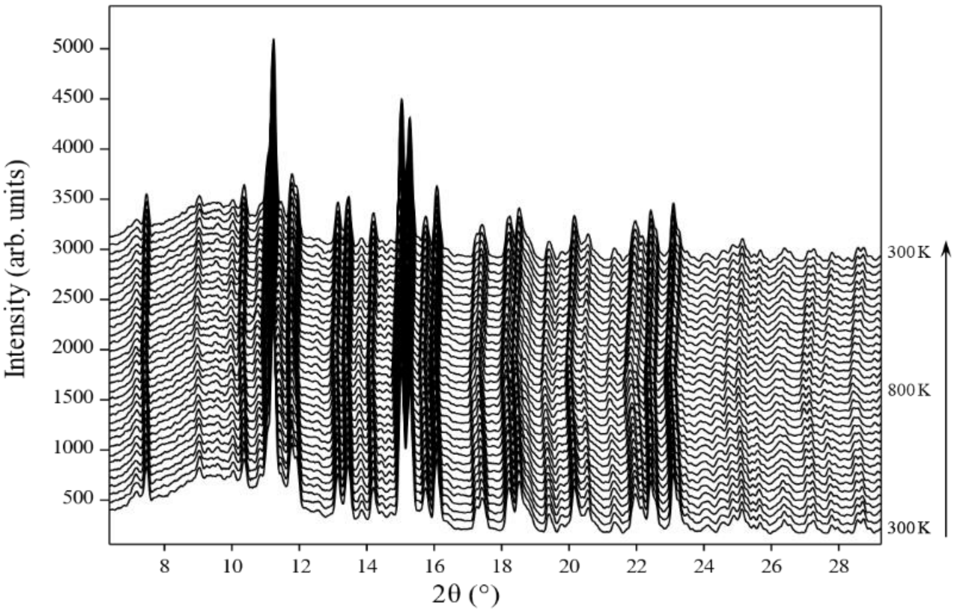

Figure 3: PXRD data of $Cr_2Sn_3S_7$ in sealed capillary as a function of the temperature (λ = 0.71073 Å)

The thermal evolution of the unit cell volume and isotropic thermal parameters is depicted in Figures 4a and 4c, respectively. These results confirm that $Cr_2Sn_3S_7$ exhibits good thermal stability under vacuum, up to at least 800 K, and shows excellent reversibility upon warming and cooling.

In the context of thermoelectricity, considering the mechanical compatibility of different components of the device is crucial. Hence, the volumetric thermal expansion coefficient was calculated using high-temperature diffraction data, assuming isotropic orientation of the crystallites. Using this approximation, a pseudo-cubic unit cell parameter a_c was derived from the actual volume data, and consequently, a linear thermal expansion coefficient α(T) (Ref. 91) as

$$\alpha(\mathrm{T}) = \frac{\partial a(T)}{\partial T} \times \frac{1}{a(T)}$$

Both volumetric ($\beta(T)$, **Figure 4(b)**) and linear ($\alpha(T)$, **Figure 4(c)**) thermal expansion coefficients of $Cr_2Sn_3S_7$ follow the same trend. These coefficients increase up to ~ 450 K, reaching a value of ~ 40.0×10^{-6} K^{-1} and 13.5×10^{-6} K^{-1}, respectively, and then remain relatively constant up to 800 K, reaching an average value between 450 K and 800 K of 44×10^{-6} K^{-1} and 14.7×10^{-6} K^{-1}, respectively. The linear thermal expansion coefficient of $Cr_2Sn_3S_7$ is comparable to other sulfide materials such as Cr_2S_3 ($\alpha(660K)$ = 12.3×10^{-6} K^{-1} (Ref 92)), $Cu_{26}Nb_2Ge_6S_{32}$ (α_{293K}^{573K} ~ 16.9×10^{-6} K^{-1} (Ref 93)), $Cu_{26}V_2Ge_6S_{32}$ (α_{600K}^{1000K} = 17.6×10^{-6} K^{-1} (Ref 94)), but much lower than the one of SnS (α_{296K}^{878K} = 37.67×10^{-6} K^{-1} (Ref 95)) which, unlike $Cr_2Sn_3S_7$, has a 2D structure.

Finally, these high temperature XRPD data reveal that isotropic thermal parameters (B_{iso}) and their thermal evolution are highly dependent on site coordination (**Figure 4(d)**). Indeed, metallic sites in an octahedral environment (*i.e.* M3, M4 and M5) exhibit a B_{iso} value and a thermal dependence equivalent to anionic sites (*i.e.* S1 to S7). Conversely, Sn^{2+} sites in three-fold coordination (*i.e.* M1 and M2) are characterized by a twice higher B_{iso} value at RT and ~2.5 times higher at 800 K. These results support the crystal chemistry investigations showing weak interactions between the guest $[Sn_4S_3]^{2+}$ chains and the $[Cr_4Sn_2S_{11}]^{2-}$ host framework.

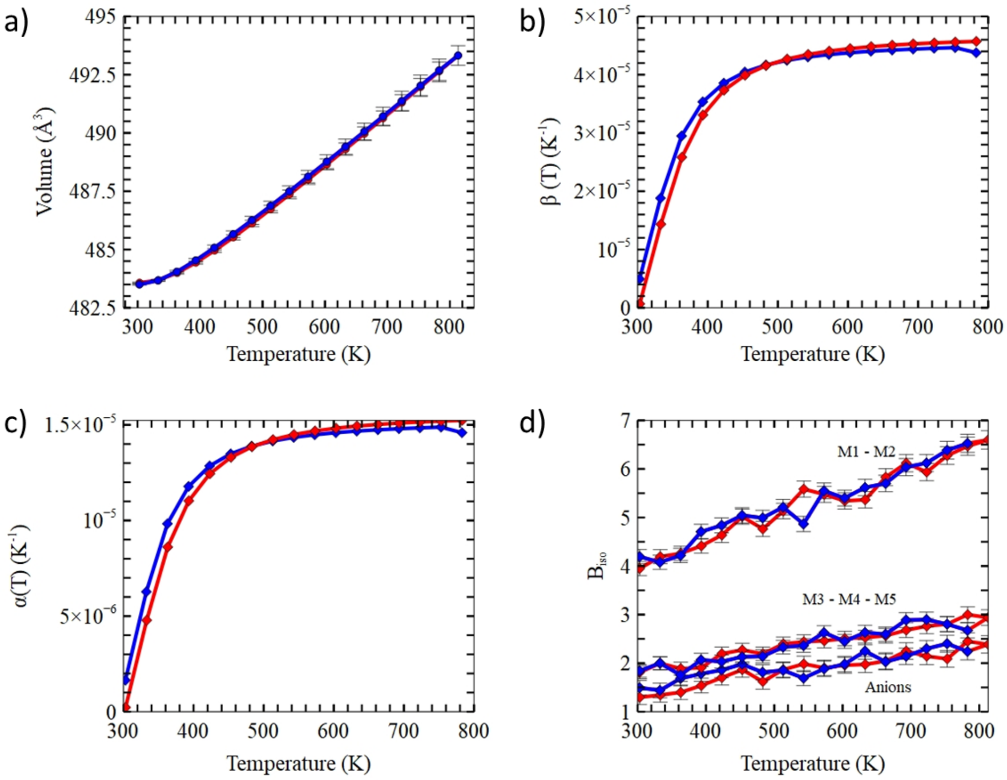

Figure 4: Temperature dependence of (a) unit cell volume, (b) volumetric thermal expansion coefficient $\beta(T)$, (c) linear thermal expansion coefficient $\alpha(T)$, and (d) refined isotropic thermal parameters (B_{iso}) of $Cr_2Sn_3S_7$ during warming (red curves) and cooling (blue curves).

^{119}Sn Mössbauer spectroscopy

As aforementioned, the formal oxidation states in $Cr_2Sn_3S_7$ are expected to be $(Cr^{3+})_2(Sn^{2+})_2(Sn^{4+})_1(S^{2-})_7$. In order to confirm the mixed oxidation state of tin in this compound, ^{119}Sn Mössbauer spectroscopy was performed. The Mössbauer spectrum recorded at 300 K evidences two absorption peaks: one with isomer shift δ = 3.72 mm s^{-1}, and the other one with δ = 1.25 mm s^{-1} (**Figure 5** and **Table 2**). Based on typical δ values of tin cations in a sulfide environment[25,90–92] these peaks can be ascribed to Sn^{2+} and Sn^{4+}, respectively.

Moreover, ^{119}Sn Mössbauer spectroscopy is a quantitative technique allowing the estimation of Sn^{2+}/Sn^{4+} ratio by measuring the area fraction of the corresponding absorption peaks. However, Lamb-Mössbauer factors are needed to convert relative spectral areas of the two components of the ^{119}Sn Mössbauer spectrum into tin abundances.[92] At RT, these factors have largely different values for Sn^{2+} and Sn^{4},$^{+93}$ explaining the higher intensity of the Sn^{4+} absorption peak at such temperature (**Figure 5** and **Table 2**), opposite to the expected Sn^{2+}/Sn^{4+} ratio in $Cr_2Sn_3S_7$. In order to estimate this ratio, it is crucial to conduct the measurement at a sufficiently low temperature to limit the difference in the absorption statistics between Sn^{2+} and Sn^{4+} (*i.e.* near the helium liquid temperature). Unfortunately, in the present case, ^{119}Sn Mössbauer spectrum recorded at 4.2 K evidences a broad signal compared to that observed at 300 K (**Figure S7**), suggesting a magnetic ordering of $Cr_2Sn_3S_7$ at low temperature. Note that the magnetic order of $Cr_2Sn_3S_7$ was confirmed by magnetic measurements (see below) and seems to occur between 40 K and 30 K (**Figure S7**). This magnetic ordering avoids an unambiguous interpretation of Mössbauer spectrum at helium liquid temperature, and consequently an accurate estimation of the Sn^{2+}/Sn^{4+} ratio. However, ^{119}Sn Mössbauer spectra recorded at several temperatures in the paramagnetic state clearly show that the signal related to Sn^{2+} dominates below 50 K and continues to increase at lower temperatures (**Figure 5** and **Table 2**). Hence, considering (i) the area fraction of the two components of the ^{119}Sn Mössbauer spectrum recorded at 40 K (*i.e.* 57% for Sn^{2+} and 43% for Sn^{4+}, **Table 2**), a temperature still far from 4.2 K, and (ii) the presence of Cr_2SnS_4 impurity in the sample (revealed by XRPD and confirmed by magnetic measurement, see below) that contains exclusively Sn in its +II oxidation state, it is reasonable to consider that the expected Sn^{2+}/Sn^{4+} ratio of 2 in $Cr_2Sn_3S_7$ is correct. This assumption is in fair agreement with area fractions of 40% and 47% assigned to Sn^{2+} signal from ^{119}Sn Mössbauer spectrum of $In_2Sn_3S_7$ samples recorded at 80 K. (Ref 82) Moreover, refinement of ^{119}Sn Mössbauer spectra of $Cr_2Sn_3S_7$ recorded at several temperatures in the paramagnetic state (**Figure 5** and **Table 2**) reveals that (i) the Sn^{2+} component is in fact a doublet with a typical linewidth and a value of quadrupole splitting (QS) of ~ 0.53 mm/s, and (ii) the Sn^{4+} component exhibits a QS value close to zero and a linewidth slightly higher than the typical one. This suggests that Sn^{4+} cations are located in sites of higher symmetry than that of Sn^{2+} cations. Hence, these results support the occupation of the strongly distorted M1 and M2 sites by the Sn^{2+} cations (*i.e.* trigonal pyramidal coordination plus five more distant sulfur atoms interacting), allowing a better accommodation of its $5s^2$ electrons, (Ref 90) the Sn^{4+} cations being mainly localized on the octahedral M3, M4 and M5 sites. Similar results and conclusions are reported by Adenis *et al.* (Ref 82) on $In_2Sn_3S_7$ indicating negligible influence of mixed cationic occupancy Cr^{3+}/Sn^{4+} on the local environment of the octahedral M3, M4, and M5 sites or a mixed occupancy also for $In_2Sn_3S_7$. Note that the none-zero QS value refined at 40 K for Sn^{4+} (**Table 2**) probably reflects the local magnetic interactions occurring just below the magnetic ordering temperature instead of a symmetry site modification. Finally, according to Lippens, (Ref 96) the isomeric shift (IS) value of ~3.77 mm/s determined for Sn in its +II oxidation state in $Cr_2Sn_3S_7$, suggests that, in this compound, this cation exhibits a valence electron density at the nucleus slightly higher at 80%. Consequently, the non-bonding doublet of $5s^2$ electrons associated to Sn^{2+} is probably hardly delocalized from the nucleus.

Table 3: ^{119}Sn hyperfine parameters of $Cr_2Sn_3S_7$: isomer shifts (IS), quadrupole splittings (QS), FWHM (Γ) and relative areas fraction (A) for the two sites of the Mössbauer spectra recorded in its paramagnetic state.

Temperature (K)	Sites	IS (mm/s) ± 0.01	QS (mm/s) ± 0.01	Γ (mm/s) ± 0.01	Area fraction (%) ± 3
300	Sn^{4+}	1.25	0.00	1.06	76
	Sn^{2+}	3.72	0.52	0.84	24
120	Sn^{4+}	1.26	0.00	1.01	55
	Sn^{2+}	3.75	0.52	0.80	45
50	Sn^{4+}	1.27	0.00	1.03	46
	Sn^{2+}	3.77	0.54	0.84	54
40	Sn^{4+}	1.28	0.40	1.07	43
	Sn^{2+}	3.77	0.53	0.93	57

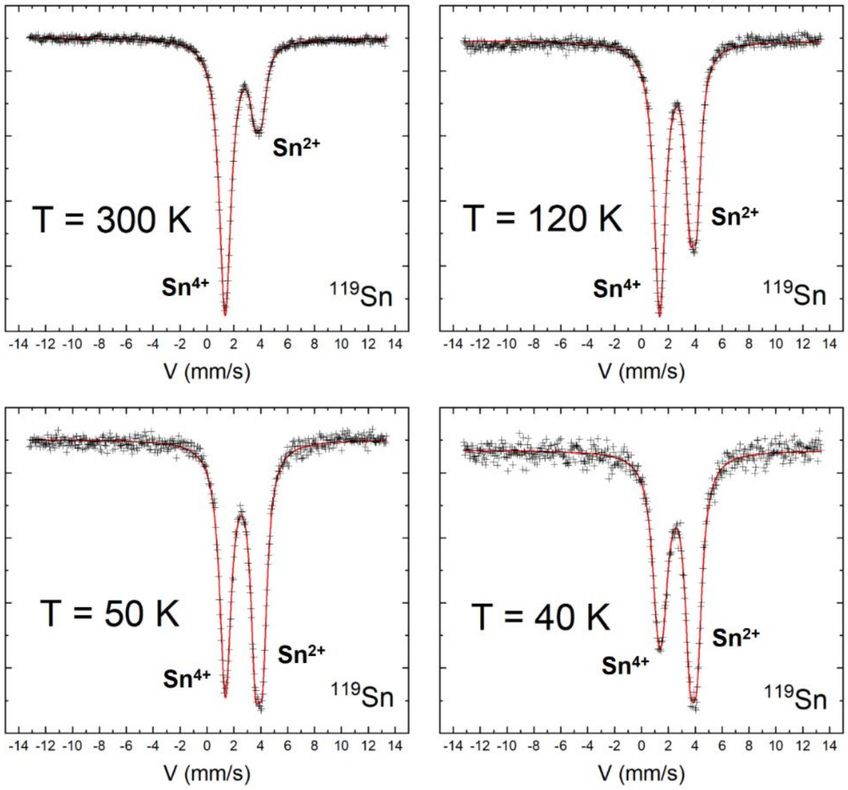

Figure 5: ^{119}Sn Mössbauer spectra (black crosses) and corresponding fits (red lines) of the $Cr_2Sn_3S_7$ sample measured at $T = 300$ K, 120 K, 50 K and 40 K.

Magnetic properties

Field-cooled magnetic susceptibility (χ) of $Cr_2Sn_3S_7$ is presented in the left part of **Figure 6**. This curve reveals at least two magnetic transitions, one at 113(2) K and the second around 36(2) K. The first magnetic transition can be assigned to the ferromagnetic ordering of the Cr_2SnS_4 impurity detected by XRPD (**Figure S2** and **Figure S8**) and the second one to the magnetic ordering of the $Cr_2Sn_3S_7$ compound itself. These interpretations are supported by the ^{119}Sn Mössbauer analyses revealing a clear magnetic ordering only between 40 K and 30 K (**Figure S7**). Unfortunately, the presence of a ferromagnetic impurity in the sample prevents a deeper interpretation of the magnetic order of $Cr_2Sn_3S_7$.

The right part of the **Figure 6** shows the temperature dependence of the inverse magnetic susceptibility ($1/\chi$), fitted with the Curie-Weiss law from 150 to 300 K. This fit leads to a paramagnetic Curie temperature θ_p of -7.1(3) K, indicating a weak predominance of antiferromagnetic interactions, and an effective magnetic moment μ_{eff} per chromium of 4.03 μ_B. This latter value is in good agreement with the spin-only magnetic moment value of Cr^{3+} ion (*i.e.* 3.87 μ_B(Ref 100)) confirming the expected formal oxidation state of chromium in $Cr_2Sn_3S_7$.

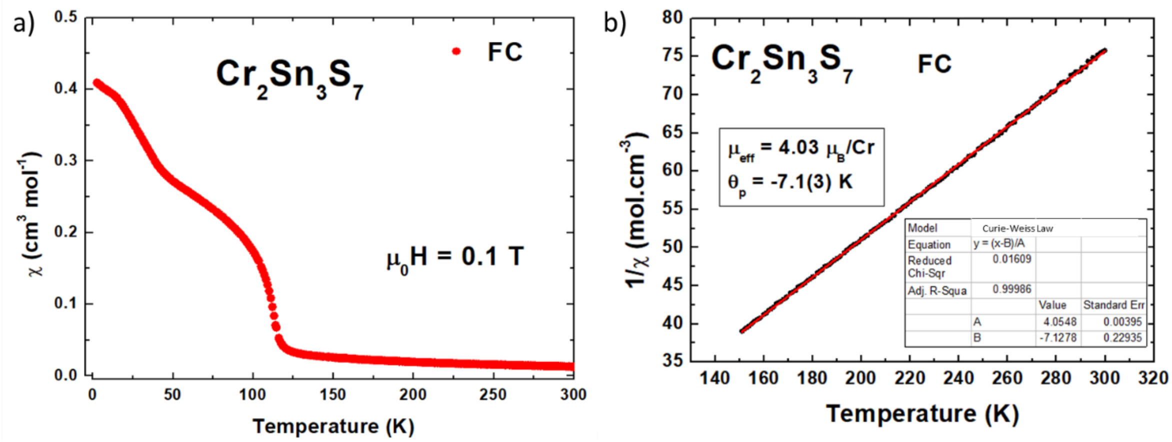

Figure 6: a) Temperature dependence of the magnetic susceptibility (χ) for $Cr_2Sn_3S_7$ recorded in field cooled (FC) mode from 300 K down to 2 K under an applied magnetic field of 0.1 T and b) inverse ($1/\chi$) corrected for diamagnetism and fitted from 150 to 300 K with the Curie-Weiss law.

Optical properties

The optical properties of $Cr_2Sn_3S_7$ have been investigated by UV–Vis spectroscopy in diffuse reflectance geometry at RT. It was converted into absorption spectrum using the Kubelka-Munk function F(R), as shown in **Figure S9**:

$$F(R) = \frac{\alpha}{K} = \frac{(1-R)^2}{2R}$$

where R is the fractional reflectance, α is the absorption coefficient, K is the scattering coefficient and *F(R)* the Kubelka-Munk function (K_m). Using the optical absorption coefficient, the optical band gap of $Cr_2Sn_3S_7$ was determined using Tauc's law. The method is based on the approximation near the absorption edge that $(F(R) \cdot E)^n = A(E - E_g)$ where E_g is the optical band gap and n a constant characterizes the transition process, (n = 2 or ½ for dipole-allowed transitions occurring at a direct or indirect band gap). Theoretical calculations (see below) show an indirect band gap for the $Cr_2Sn_3S_7$ (n = ½). The fits of the Tauc plot are shown in **Figure S9**. The curve has a good straight line fit over a higher energy range above the absorption edge, indicative of an indirect optical transition near the absorption edge. The linear fit leads to an extremely narrow band gap of ~0.16 eV. Such value is significantly lower with respect to the binary compounds SnS (1.34 eV (Ref 101)) and Cr_2S_3 (0.45 eV (Ref 102)). This difference could be ascribed to the important cations mixing (Sn^{2+} *vs* Sn^{4+}/Cr^{3+}) or by a confinement effect of the CdI_2 layer as suggested by a similar band gap found for a Cr_2S_3 multilayers. (Ref 103)

Transport properties and further analyses by *ab initio* calculations

The optimized structures of the three ordered models and the semi-ordered model (See experimental section and **Figure S10**) are slightly distorted due to non-uniform arrangements of Sn and Cr at M3, M4 and M5 sites. The internal energies of the three ordered models are lower than that of the semiordered model by 10.7, 7.9, and 11.8 meV/atom, with their variations being as small as the thermal energy of an atom at 27 K. A slightly higher internal energy of the semiordered model would be readily overcome by the entropy term at finite temperature, supporting the stability of the partial occupancy of the cations at those sites at finite temperature from a thermodynamic viewpoint. Effective charges of Sn atoms in the ordered (semiordered) structure, calculated using Bader population analysis (Ref 104), confirm the mixed valence of Sn^{2+} and Sn^{4+} in this compound.

Figure 7 shows the electron localization function (ELF), which can intuitively display lone electron pairs(Ref 105), for an ordered model in comparison with SnS. Due to interaction with the surrounding 8 S atoms, the lone electron pair of Sn^{2+} in the $Cr_2Sn_3S_7$ model is less directional compared to the lone pair in SnS and remains close to the nucleus, as shown by Mössbauer spectroscopy.

Figure 8 shows the calculated electronic band structure and DOS curves near the Fermi level of the semiordered and ordered models. Orbitals of Cr, Sn, and S contribute to forming the bottom of conduction bands and the top of valence bands. Indirect band gaps are small or almost closed, in agreement with the experiment (see optical properties). On the other hand, direct band gaps in the ordered models are substantial in any model. This suggests that electrons cannot be excited alone, at least locally, without interaction with phonons, for example, and thus, a doping strategy for better electronic conduction needs to be carefully considered, although it is beyond the scope of this study.

The temperature dependence of the electrical resistivity (ρ) is shown in Figure S11. In agreement with optical properties and band structure calculations, the ρ(T) curve follows a nondegenerate semiconducting behavior with values decreasing from 0.025 Ω·m at 325 K to 0.004 Ω·m at 673 K. The high electrical resistivity in our sample is consistent with its relatively high Seebeck coefficient (S) of around -350 $\mu V \cdot K^{-1}$ at RT (Figure S11). The carrier concentration measured at RT is equal to 3.75×10^{18} cm^{-3}, which is consistent with the ρ and S values. The calculated carrier mobility at RT is equal to 0.6 $cm^2 \cdot V^{-1} \cdot s^{-1}$. Such a low value is mainly explained by the disorder (point defects) due to the mixed cationic occupancy in the $[Cr_4Sn_2S_{11}]^{2-}$ host framework

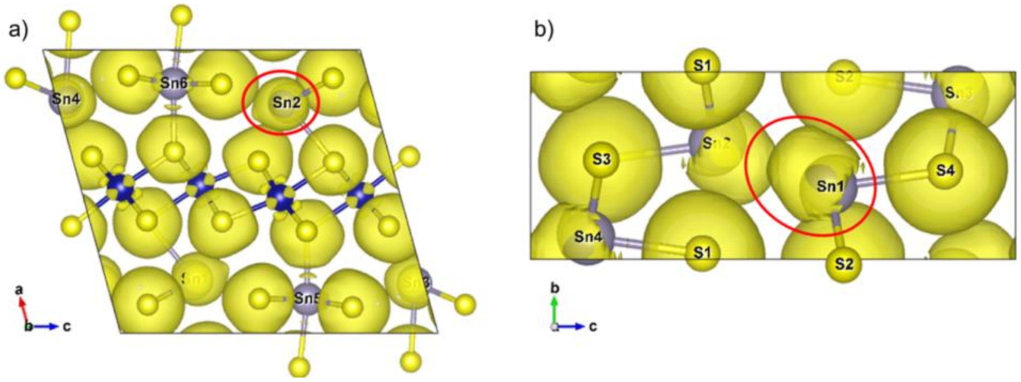

Figure 7. ELF isosurface at 0.21 of the (a) Cr2Sn3S7 model in comparison with (b) SnS. A lone electron pair of Sn2+ is circled in red.

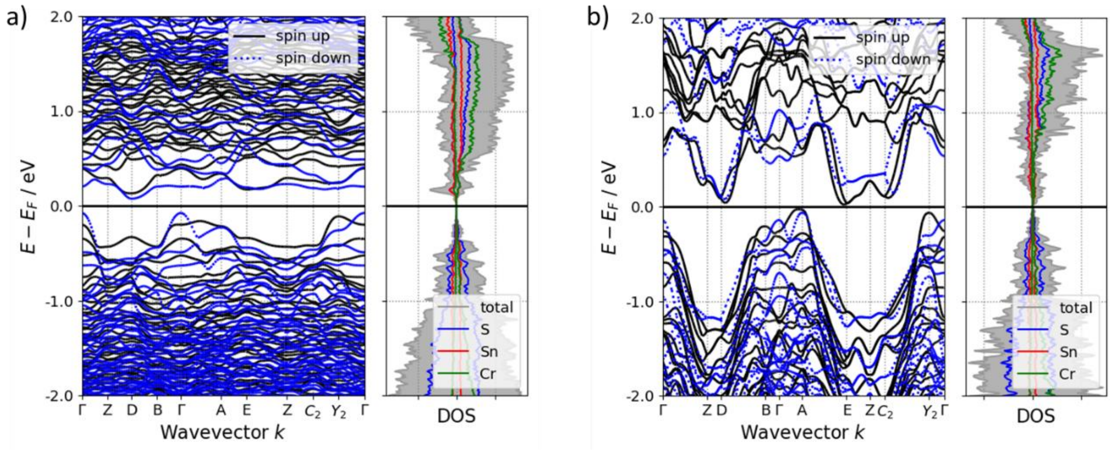

Figure 8: Electronic band structures and density of states (DOSes) of (a) semi-order model and (b) one ordered model. Two other ordered models are in **Figure S12**.

Thermal properties

$Cr_2Sn_3S_7$ exhibits a low lattice thermal conductivity ($\kappa \approx \kappa L$ due to the negligible electronic contribution) of 0.77 $W \cdot m^{-1} \cdot K^{-1}$ at 325 K, which slightly decreases as the temperature increases, reaching 0.69 $W \cdot m^{-1} \cdot K^{-1}$ at 673 K (Figure 9). The same magnitude of κL is reported in SnS, which shares common structural features with $Cr_2Sn_3S_7$. Note that there is a correlation between the crystal structures (i.e., Sn. environment and oxidation state) and κ_L in Sn-rich sulfides is discussed in the last paragraph of this section.

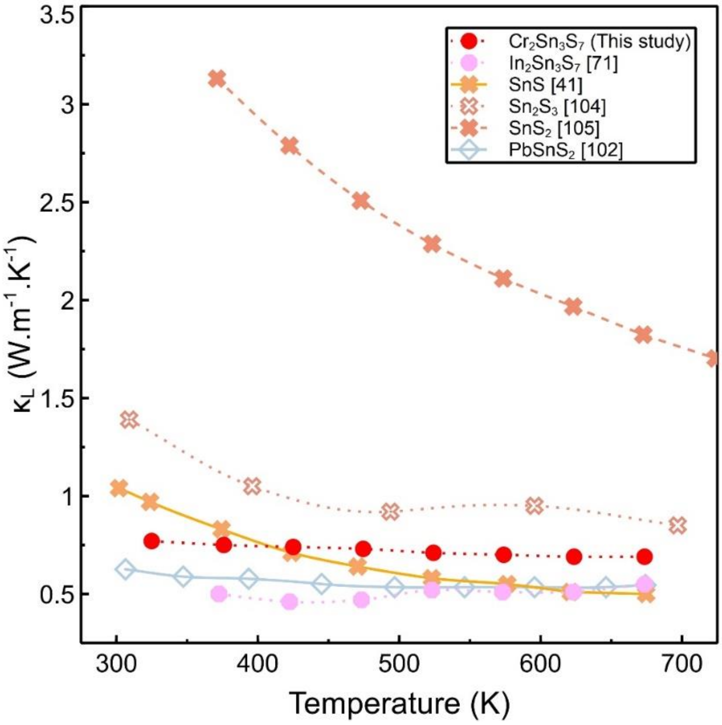

Figure 9: Lattice thermal conductivity from 300 to 700K in Sn-rich sulfides. The full lines correspond to compounds with only Sn^{2+}, dotted lines to compounds with Sn^{2+} and Sn^{4+}, and dashed lines to compounds constituted of only Sn^{4+}.

We have carried out heat capacity, C_p (2-280 K) measurements to understand the ultralow κ_L in $Cr_2Sn_3S_7$ (**Figure S13a**). We observed that the plot of C_p/T vs. T^2 can be well fitted by a combination of the Debye and Einstein models rather than the Debye model alone in the temperature range of 2-50 K (**Figure S13b**) and the combined Debye-Einstein model can be expressed as: (Ref 106, 107)

$$\frac{C_p}{T} = \gamma + \beta T^2 + \sum_n \left(A_n \left(\theta_{E_n}\right)^2 . (T^2)^{-3/2} . \frac{e^{\theta_{E_n}/T}}{\left(e^{\theta_{E_n}/T} - 1\right)^2} \right)$$

Where γ is define as Sommerfeld coefficient (represent the electronic contribution), β depicts the lattice contribution. The third term in the equation is Einstein oscillators corresponding to the localized lattice vibrations (A_n is the prefactor and θ_{E_n} is the Einstein temperature of the nth Einstein oscillator mode). We have observed a good fit using this Debye-Einstein model with three Einstein mode of θ_{E_1}= 14 K (10 cm^{-1}), θ_{E_2}= 50 K (35 cm^{-1}) and, θ_{E_3}= 115 K (80 cm^{-1}) (**Figure S13b**). These low energy Einstein modes can be attributed to the localized vibration of Sn (M1, M2) atoms (**Figure 10**). These low energy optical phonon modes strongly interact with the heat carrying acoustic phonon modes which inhibits the phonon propagation through the lattice resulting in very low κ_L in $Cr_2Sn_3S_7$.

To further shed light on the origin of low κ_L in $Cr_2Sn_3S_7$, we have performed DFT calculations of phonon band structures and element-deconvoluted DOSes of the semi-ordered and ordered models, as shown in **Figure 10**. For Sn, DOSes are further decomposed to the one for M1 and M2 sites (*i.e.* Sn^{2+}) and the one for the three other cationic sites (*i.e.* Sn^{4+}, M3, M4 and M5). It was found that Sn cations vibrate at low frequency region while S and Cr ions vibrate at intermediate and high frequency regions, reflecting their atomic masses (52.0 g/mol for Cr, 118.7 g/mol for Sn, and 32.1 g/mol for S). Among Sn cations, the ones at M1 and M2 sites (*i.e.* Sn^{2+}) with lone pairs of electrons mainly contribute to lower frequency bands including acoustic modes. On the other hand, Sn^{4+} cations at M3, M4 and M5 sites are more coupled with Cr^{3+} and S^{2-} up to 6 THz. The overlap of partial DOSs of Cr and S, especially at high frequencies, implies coupled vibrations between them. Overall, the dispersion of bands is rather flat, corresponding to small group velocities. **Figure 11a** shows probable atomic displacements calculated for the semiordered model within the harmonic approximation. Unsurprisingly, Sn^{2+} cations at M1 and M2 sites exhibit a rather ellipsoidal shape of atomic vibrations, deviating more from a perfect sphere than ions at other sites. Thermal displacements of Sn^{4+} and Cr^{3+} at other sites (M3, M4, and M5), along with those of S^{2-}, are also ellipsoidal but to a much lesser extent. These disoriented atomic vibrations deteriorate the coupled vibrations of atoms.

The large calculated atomic displacements of Sn^{2+} in M1 and M2 sites align well with the large anisotropic atomic displacement parameters (ADP) determined from SCXRD (**Figure 11b).** As shown in Table S4, the ADP values at M1 and M2 sites are significantly larger compared to those at M3, M4, and M5 sites. Note also that the shapes of the ellipsoids and the magnitudes of vibration are in excellent agreement with both experimental and theoretical data (**Figure 11**). These results confirm that the unique atomic arrangement and weak chemical bonding of the guest $[Sn_4S_3]^{2+}$ chains to the $[Cr_4Sn_2S_{11}]^{2-}$ host framework provide a permissive environment for strong oscillations of Sn^{2+} cations. Such rattling behavior associated to lattice anharmonicity induced by the lone pair of Sn^{2+} results in ultralow thermal conductivity in $Cr_2Sn_3S_7$.

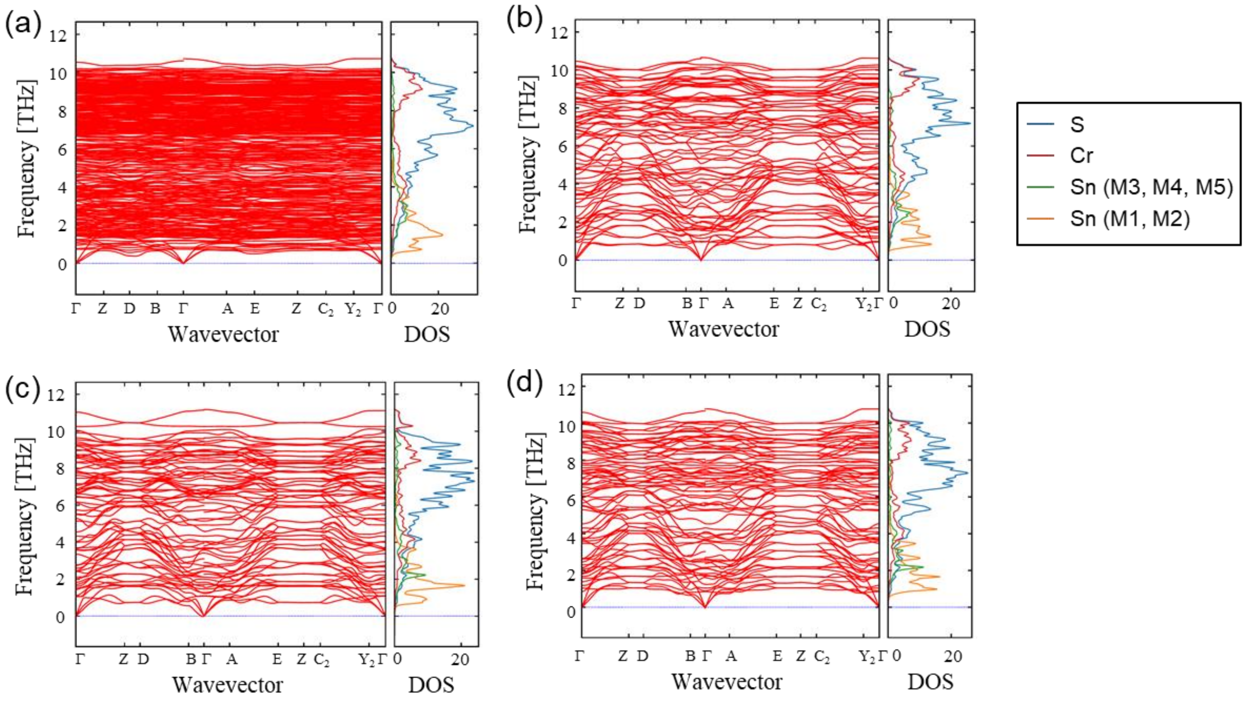

Figure 10: Phonon band structures and density of states (DOSes) of (a) semi-orderer model and (b,c,d) three ordered models. Partial DOS of Sn at M1 and M2 sites (in orange) are separated from that at M3, M4 and M5 sites (in green).

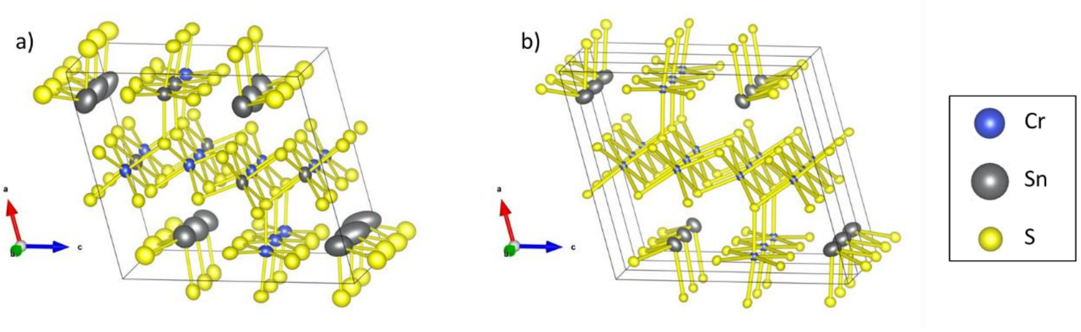

Figure 11: (a) Thermal displacement ellipsoids of ions at 1000 K in the semi-ordered model, and (b) anisotropic atomic displacement parameters determined through single crystal X-ray diffraction. To facilitate comparison, the experimental results are presented for 3 unit cells along the b-axis. The ellipsoids are depicted at the 50% probability level.

To better understand how the phonons determine thermal conductivity, Cv^2 of the semi-ordered and ordered models were calculated as a function of frequency, ω (**Figure S15**). Lattice thermal conductivity κ can be calculated according to the equation:

$$\kappa = \int C_{\mathrm{V}}(\omega) v_{\mathrm{g}}^2(\omega) \tau(\omega)$$

where $C_{\mathrm{V}}(\omega)$ is the constant-volume heat capacity, $v_{\mathrm{g}}(\omega)$ is group velocity, $\tau(\omega)$ is the relaxation time as a function of frequency, ω. Thus, Cv^2 corresponds to the thermal conductivity when the phonon relaxation time is assumed to be unity independent of frequency, thus giving an estimate of the thermal conductivity. In the **Figure S15**, Cv^2 of the ordered models are divided by that of the semi-ordered model while Cv^2 of the semi-ordered model is indicated by a dotted line at $Cv^2 = 1$. Curves of the three ordered models deviate from one another, indicating that the phonon states differ due to partial occupancies of Cr and Sn cations and associated local distortions. All of them are higher than unity. In other words, Cv^2 of the semi-ordered model is lower than those of the ordered model by factors of magnitude, even though local composition in the parallelepiped of ca. 1 nm along each axis is the same. Heat capacity barely changes when local composition and its crystal structure remain the same. Thus, the significant change in Cv^2 of the semi-ordered model as compared to those of the ordered model can be attributed to the change in the group velocities of phonons which can be seen in **Figure 10**. It is no doubt that phonon relaxation time or phonon mean free path is shortened when spatial distributions of Cr and Sn cations are more randomized due to the partial occupancies of the cations. This suggests that the cationic disorder in the $[Cr_4Sn_2S_{11}]^{2-}$ host framework probably also contributes to the low lattice thermal conductivity of $Cr_2Sn_3S_7$. Mode Grüneisen parameters, which show phonon anharmonicity due to volume change,(Ref 108) of the ordered model are shown in **Figure 12** as a function of frequency, there is a peak of 30 at around 1 THz, coinciding with peaks in Sn^{2+} phonon DOS, while the values converge to 1 at higher frequencies. This indicates that, despite being acoustic phonons, Sn^{2+} vibrations exhibit anisotropy 30 times stronger than that of optical phonons. This underscores the role of Sn^{2+} in reducing the lattice thermal conductivity of $Cr_2Sn_3S_7$, a phenomenon that would similarly apply to the semiordered model.

From our experimental and theorical investigations, we succeeded to disentangle the origin of low thermal conductivity (0.77 W m^{-1} K^{-1} @ 325 K, **Figure 9**) in $Cr_2Sn_3S_7$. The crystal structure of this compound is rather complex, and comprises two sub-networks weakly bonded one to another, as discussed earlier. Those weak interactions are induced by the stereo-chemical activity of Sn^{2+} and is mainly governed by the presence of SnS_3L chains of tetrahedrons. The lattice softening, vibration and anharmonicity at the origin of the low thermal conductivity are directly related the presence of Sn^{2+} in the structure. This is also verified in SnS and $PbSnS_2$ (constituted of Sn in only 2+ oxidation state) which exhibit low thermal conductivity of 1.04 W m^{-1} K^{-1} and 0.51 W m^{-1} K^{-1} at 300 K (**Figure 9**) (Refs. 39, 41, 48, 109).

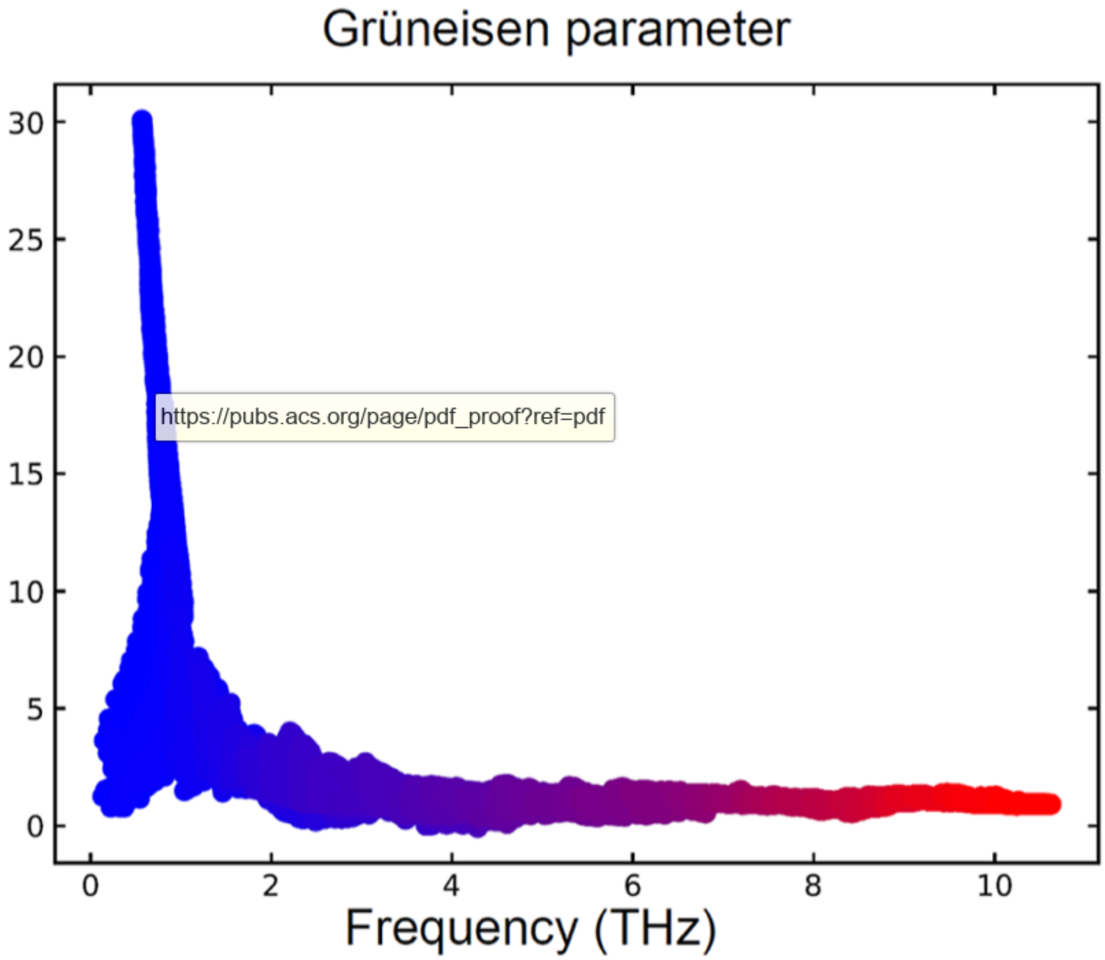

Figure 12. Calculated mode Grüneisen parameters of an ordered model

Bearing in mind that, in SnS and isostructural $PbSnS_2$, each Sn^{2+}/Pb^{2+} cation exhibits a tetrahedral coordination PbS_3L or SnS_3L similar to that observed for Sn^{2+} in $Cr_2Sn_3S_7$, we can describe the 2D crystal structure of SnS and $PbSnS_2$ as the stacking along the *c*-axis of puckered [$PbSnS_2$] layers built up of corner-sharing (Pb,Sn)S_3L tetrahedra, with very weak interlayer interactions between the Pb^{2+} or Sn^{2+}cations of two consecutive layers. (Ref 109) This lattice softening explains the extremely low thermal conductivity of SnS and $PbSnS_2$. Note that $PbSnS_2$ has κ_L values substantially lower compared to SnS, due to additional cationic disorder in the former compound. The key role of Sn^{2+} on the generation of low thermal conductivity is further evidenced by the increasing trend of κ_L from SnS (1.04 W m^{-1} K^{-1} at 300 K), (Ref 48) to Sn_2S_3 (1.39 W m^{-1} K^{-1} at 310 K) (Ref 110) and SnS_2 (3.13 W m^{-1} K^{-1} at 370 K)(Ref 111) also suggests that there is a correlation between the presence of Sn^{2+} and the generation of low thermal conductivity (**Figure 9**). While SnS is only constituted of Sn^{2+} in layers built up of corner-sharing SnS_3L tetrahedra, Sn_2S_3 contains both Sn^{2+} and Sn^{4+} and the structure ~~is~~ consists of 1D chains of ~~six-coordinate~~ $Sn^{4+}S_6$ octahedra capped by tetrahedral Sn^{2+}, with one anionic ~~coordination~~ site occupied by the lone pair L ($Sn^{2+}S_3L$, similar to the $Cr_2Sn_3S_7$). In contrast, SnS_2 contains only ~~of~~ Sn^{4+}located in CdI_2-type edge shared octahedra layers. J. Skelton *et al.*[105], based on theoretical investigations, confirm the lower magnitudes of lattice thermal conductivity in SnS and Sn_2S_3 compared to SnS_2 as reported in experimental results.

Conclusions

We have demonstrated that high-purity $Cr_2Sn_3S_7$ can be prepared by ceramic method and spark plasma sintering. The analysis of the structure shows that $Cr_2Sn_3S_7$ can be described by two sub-lattices, one host constituted of $[Cr^{3+}{}_4Sn_2{}^{4+}S_{11}]^{2-}$ entities forming tunnels where guest $[Sn^{2+}{}_4S_3]^{2+}$ chains containing lone pair electrons cations are located. We have determined that this sulfide is magnetically ordered at low temperature and exhibits a *n*-type semiconducting behavior with a low energy band gap and low thermal and electrical conductivities. By combining experiments and theory, we succeeded in disentangling the origin of low κ_L in $Cr_2Sn_3S_7$. The presence of Sn^{2+} induces weak bonds between the chains and host framework, leading to ~~which induces~~ lattice softening and associated low frequency vibrations including acoustic modes. The present investigation highlights ~~on~~ the fundamental role of Sn^{2+} in the generation of low lattice thermal conductivity in sulphides and opens new perspectives for the exploration of ~~transition~~ metal sulphides characterized by the coexistence of both, strong and weak chemical bonds in the same matrix. ~~constituted of weakly bonded cationic frameworks~~. In particular, pointing to the construction on the existence of crystal structures composed of multiple subunits with decoupled vibrational properties.

AUTHOR INFORMATION

Corresponding Author

Carmelo Prestipino – Univ. Rennes, CNRS, ISCR-UMR 6226, F-35000 Rennes, France; orcid.org/0000-0002-8541-7766; Email: carmelo.prestipino@univ-rennes.fr

Pierric Lemoine - Institut Jean Lamour, UMR 7198, CNRS, Université de Lorraine, 54011 Nancy, France; orcid.org/0000-0002-3465-7815; Email: pierric.lemoine@univ-lorraine.fr

Present Addresses

†If an author's address is different than the one given in the affiliation line, this information may be included here.

Author Contributions

The manuscript was written through contributions of all authors. All authors have given approval to the final version of the manuscript. ‡These authors contributed equally. (match statement to author names with a symbol)

Funding Sources

Any funds used to support the research of the manuscript should be placed here (per journal style).

Notes

Any additional relevant notes should be placed here.

ACKNOWLEDGMENTS

The authors gratefully thank T. Guizouarn, A. Panaget, C. Desbordes, J. Lecourt, and C. Bilot for their technical contribution. The authors acknowledge SOLEIL (Saint-Aubin, France) for the provision of synchrotron radiation facilities.

REFERENCES

1. Rakspun, J.; Kantip, N.; Vailikhit, V.; Choopun, S.; Tubtimtae, A. Multi-Phase Structures of Boron-Doped Copper Tin Sulfide Nanoparticles Synthesized by Chemical Bath Deposition for Optoelectronic Devices. *J. Phys. Chem. Solids* **2018**, *115*, 103−112.
2. Li, R.-A.; Zhou, Z.; Lian, Y.-K.; Jia, F.; Jiang, X.; Tang, M.-C.; Wu, L.-M.; Sun, J.; Chen, L. A_2SnS_5: A Structural Incommensurate Modulation Exhibiting Strong Second-Harmonic Generation and a High Laser-Induced Damage Threshold (A = Ba, Sr). *Angew. Chem., Int. Ed.* **2020**, *59* (29), 11861−11865.
3. Bavar, S. M. R.; Alamolhoda, S.; Bafghi, M. S.; Masoudpanah, S. M. Photocatalytic Performances of Cobalt Sulfides Prepared by Solution Combustion Synthesis Using Mixed Fuels. *J. Phys. Chem. Solids* **2021**, *149*, 109805.
4. Breton, L. S.; Morrison, G.; zur Loye, H. C. Synthesis, Characterization, and Magnetic Properties of Uranium-Containing 2H-Perovskite-Related Sulfides: Ba_3MUS_6 (M = Mn, Fe, Co, Ni) and $Ba_3Co_{0.858(5)}Mg_{0.142(5)}US_6$. *Inorg. Chem.* **2023**, *62* (42), 17409−17416.
5. Sadan, M. K.; Jeon, M.; Yun, J.; Song, E.; Cho, K.-K.; Ahn, J.-H.; Ahn, H.-J. Excellent Electrochemical Performance of a Mesoporous Nickel Sulfide Anode for Na/K-Ion Batteries. *ACS Appl. Energy Mater.* **2021**, *4* (12), 14537−14545.
6. Hartmann, F.; Benkada, A.; Indris, S.; Poschmann, M.; Lü hmann, H.; Duchstein, P.; Zahn, D.; Bensch, W. Directed Dehydration as Synthetic Tool for Generation of a New Na_4SnS_4 Polymorph: Crystal Structure, Na^+ Conductivity, and Influence of Sb-Substitution. *Angew. Chem., Int. Ed.* **2022**, *61* (36), No. e202202182.
7. Liu, Y.-Y.; Xu, L.; Guo, X.-T.; Lv, T.-T.; Pang, H. Vanadium Sulfide Based Materials: Synthesis, Energy Storage and Conversion. *J. Mater. Chem. A* **2020**, *8* (40), 20781−20802.

8. Delacotte, C.; Pomelova, T. A.; Stephant, T.; Guizouarn, T.; Cordier, S.; Naumov, N. G.; Lemoine, P. $NaGdS_2$: A Promising Sulfide for Cryogenic Magnetic Cooling. *Chem. Mater.* **2022**, *34* (4), 1829−1837.
9. Noguchi, H.; Setiyadi, A.; Tanamura, H.; Nagatomo, T.; Omoto, O. Characterization of Vacuum-Evaporated Tin Sulfide Film for Solar Cell Materials. *Sol. Energy Mater. Sol. Cells* **1994**, *35*, 325−331.
10. Berg, D. M.; Djemour, R.; Gü tay, L.; Zoppi, G.; Siebentritt, S.; Dale, P. J. Thin Film Solar Cells Based on the Ternary Compound Cu_2SnS_3. *Thin Solid Films* **2012**, *520* (19), 6291−6294.
11. Bourgeois, C.; Bouyrie, Y.; Supka, A. R.; Al Rahal Al Orabi, R.; Lemoine, P.; Lebedev, O. I.; Ohta, M.; Suekuni, K.; Nassif, V.; Hardy, V.; Daou, R.; Miyazaki, Y.; Fornari, M.; Guilmeau, E. High-Performance Thermoelectric Bulk Colusite by Process Controlled Structural Disordering. *J. Am. Chem. Soc.* **2018**, *140* (6), 2186−2195.
12. Long, S. O. J.; Powell, A. V.; Vaqueiro, P.; Hull, S. High Thermoelectric Performance of Bornite through Control of the Cu(II) Content and Vacancy Concentration. *Chem. Mater.* **2018**, *30* (2), 456−464.
13. Jia, F.; Zhao, S.; Wu, J.; Chen, L.; Liu, T.-H.; Wu, L.-M. Cu_3BiS_3: Two-Dimensional Coordination Induces Out-of-Plane Phonon Scattering Enabling Ultralow Thermal Conductivity. *Angew. Chem., Int. Ed.* **2023**, *62* (51), No. e202315642.
14. Nolas, G. S.; Sharp, J.; Goldsmid, H. J. *Thermoelectrics: Basic Principles and New Materials Developments*; Hull, R., Osgood, R. M., Sakaki, H., Zunger, A., Eds.; Springer Series in MATERIALS SCIENCE; Springer: Berlin, Heidelberg, 2001; Vol. 45. DOI: .

15. Lemoine, P.; Guélou, G.; Raveau, B.; Guilmeau, E. Crystal Structure Classification of Copper-Based Sulfides as a Tool for the Design of Inorganic Functional Materials. *Angew. Chem., Int. Ed.* **2022**, *61* (2), No. e202108686.

16. Suekuni, K.; Tsuruta, K.; Kunii, M.; Nishiate, H.; Nishibori, E.; Maki, S.; Ohta, M.; Yamamoto, A.; Koyano, M. High-Performance Thermoelectric Mineral $Cu_{12-x}Ni_xSb_4S_{13}$ Tetrahedrite. *J. Appl. Phys.* **2013**, *113* (4), 043712.

17. Lu, X.; Morelli, D. T. Natural Mineral Tetrahedrite as a Direct Source of Thermoelectric Materials. *Phys. Chem. Chem. Phys.* **2013**, *15* (16), 5762−5766.

18. Lu, X.; Morelli, D. T.; Xia, Y.; Zhou, F.; Ozolins, V.; Chi, H.; Zhou, X.; Uher, C. High Performance Thermoelectricity in Earth-Abundant Compounds Based on Natural Mineral Tetrahedrites. *Adv. Energy Mater.* **2013**, *3* (3), 342−348.

19. Chetty, R.; S, P. K. D.; Rogl, G.; Rogl, P.; Bauer, E.; Michor, H.; Suwas, S.; Puchegger, S.; Giester, G.; Mallik, R. C. Thermoelectric Properties of a Mn Substituted Synthetic Tetrahedrite. *Phys. Chem. Chem. Phys.* **2015**, *17* (3), 1716−1727.

20. Guélou, G. P. L.; Powell, A. V.; Smith, R. I.; Vaqueiro, P. The Impact of Manganese Substitution on the Structure and Properties of Tetrahedrite. *J. Appl. Phys.* **2019**, *126* (4), 045107.

21. Kim, F. S.; Suekuni, K.; Nishiate, H.; Ohta, M.; Tanaka, H. I.; Takabatake, T. Tuning the Charge Carrier Density in the Thermoelectric Colusite. *J. Appl. Phys.* **2016**, *119* (17), 175105.

22. Guélou, G.; Lemoine, P.; Raveau, B.; Guilmeau, E. Recent Developments in High-Performance Thermoelectric Sulphides: An Overview of the Promising Synthetic Colusites. *J. Mater. Chem. C* **2021**, *9* (3), 773−795.

23. Pavan Kumar, V.; Supka, A. R.; Lemoine, P.; Lebedev, O. I.; Raveau, B.; Suekuni, K.; Nassif, V.; Al Rahal Al Orabi, R.; Fornari, M.; Guilmeau, E. High Power Factors of

Thermoelectric Colusites $Cu_{26}T_2Ge_6S_{32}$ (T = Cr, Mo, W): Toward Functionalization of the Conductive "Cu−S" Network. *Adv. Energy Mater.* **2019**, *9* (6), 1803249.

24. Hagiwara, T.; Suekuni, K.; Lemoine, P.; Supka, A. R.; Chetty, R.; Guilmeau, E.; Raveau, B.; Fornari, M.; Ohta, M.; Al Rahal Al Orabi, R.; Saito, H.; Hashikuni, K.; Ohtaki, M. Key Role of D_0 and D_{10} Cations for the Design of Semiconducting Colusites: Large Thermoelectric ZT in $Cu_{26}Ti_2Sb_6S_{32}$ Compounds. *Chem. Mater.* **2021**, *33* (9), 3449−3456.
25. Zhang, R.; Chen, K.; Du, B.; Reece, M. J. Screening for Cu−S Based Thermoelectric Materials Using Crystal Structure Features. *J. Mater. Chem. A* **2017**, *5* (10), 5013−5019.
26. Pavan Kumar, V.; Barbier, T.; Caignaert, V.; Raveau, B.; Daou, R.; Malaman, B.; Caër, G. L.; Lemoine, P.; Guilmeau, E. Copper Hyper-Stoichiometry: The Key for the Optimization of Thermoelectric Properties in Stannoidite $Cu_{8+x}Fe_{3-x}Sn_2S_{12}$. *J. Phys. Chem. C* **2017**, *121* (30), 16454−16461.
27. Shen, Y.; Li, C.; Huang, R.; Tian, R.; Ye, Y.; Pan, L.; Koumoto, K.; Zhang, R.; Wan, C.; Wang, Y. Eco-Friendly p-Type Cu_2SnS_3 Thermoelectric Material: Crystal Structure and Transport Properties. *Sci. Rep.* **2016**, *6* (1), 32501.
28. Tan, Q.; Sun, W.; Li, Z.; Li, J.-F. Enhanced Thermoelectric Properties of Earth-Abundant Cu_2SnS_3 via In Doping Effect. *J. Alloys Compd.* **2016**, *672*, 558−563.
29. Raveau, B. Copper Mixed Valence Concept: "Cu(I)−Cu(II)" in Thermoelectric Copper Sulfides—an Alternative to "Cu(II)−Cu(III)" in Superconducting Cuprates. *J. Supercond. Nov. Magnetism* **2020**, *33*, 259−263.
30. Caballero-Calero, O.; Ares, J. R.; Martín-González, M. Environmentally Friendly Thermoelectric Materials: High Performance from Inorganic Components with Low Toxicity and Abundance in the Earth. *Adv. Sustainable Syst.* **2021**, *5*, 2100095.

31. Bourgeois, C.; Lemoine, P.; Lebedev, O. I.; Daou, R.; Hardy, V.; Malaman, B.; Guilmeau, E. Low Thermal Conductivity in Ternary $Cu_4Sn_7S_{16}$ Compound. *Acta Mater.* **2015**, *97*, 180−190.

32. Cui, J.; He, T.; Han, Z.; Liu, X.; Du, Z. Improved Thermoelectric Performance of Solid Solution $Cu_4Sn_{7.5}S_{16}$ through Isoelectronic Sub

33. Pavan Kumar, V.; Lemoine, P.; Carnevali, V.; Guélou, G.; Lebedev, O. I.; Boullay, P.; Raveau, B.; Al Rahal Al Orabi, R.; Fornari, M.; Prestipino, C.; Menut, D.; Candolfi, C.; Malaman, B.; Juraszek, J.; Guilmeau, E. Ordered Sphalerite Derivative Cu5_55Sn2_22 S7_77: A Degenerate Semiconductor with High Carrier Mobility in the Cu−Sn−S Diagram. *J. Mater. Chem. A* **2021**, *9* 10812−10826.

34. Guélou, G.; Pavan Kumar, V.; Carnevali, V.; Lebedev, O. I.; Raveau, B.; Couder, C.; Prestipino, C.; Lemoine, P.; Malaman, B.; Juraszek, J.; Candolfi, C.; Lenoir, B.; Al Rahal Al Orabi, R.; Fornari, M.; Guilmeau, E. Long-Range Cationic Order Collapse Triggered by S/Cl Mixed-Anion Occupancy Yields Enhanced Thermoelectric Properties in Cu5_55Sn2_22S7_77. *Chem. Mater.* **2021**, *33* 9425−9438.

35. Kumar, V. P.; Lemoine, P.; Carnevali, V.; Guélou, G.; Lebedev, O. I.; Raveau, B.; Al Rahal Al Orabi, R.; Fornari, M.; Candolfi, C.; Prestipino, C.; Menut, D.; Malaman, B.; Juraszek, J.; Suekuni, K.; Guilmeau, E. Local-Disorder-Induced Low Thermal Conductivity in Degenerate Semiconductor Cu22_{22}22Sn10_{10}10S32_{32}32. *Inorg. Chem.* **2021**, *60* 16273−16285.

36. Lemoine, P.; Raveau, B.; Boullay, P.; Guilmeau, E.; Deng, T.; Xing, T.; Brod, M. K.; Sheng, Y.; Qiu, P.; Veremchuk, I.; Song, Q.; Wei, T.-R.; Yang, J.; Snyder, G. J.; Grin, Y.; Chen, L.; Shi, X. Comment on the "Discovery of High-Performance Thermoelectric Copper Chalcogenide Using Modified Diffusion-Couple High-Throughput Synthesis and Automated Histogram Analysis Technique." *Energy Environ. Sci.* **2020**, *13* 3041.

37. Chen, X.; Ning, S.; Yu, T.; Qu, X.; Qi, N.; Chen, Z. Optimization of Carrier Concentration in Cu22_{22}22Sn10_{10}10S32_{32}32 through In- and Zn-Doping for Enhanced Thermoelectric Performance. *ACS Appl. Energy Mater.* **2024**, *7* 508−516.
38. Guo, R.; Wang, X.; Kuang, Y.; Huang, B. First-Principles Study of Anisotropic Thermoelectric Transport Properties of IV-VI Semiconductor Compounds SnSe and SnS. *Phys. Rev. B* **2015**, *92* 115202.
39. He, W.; Wang, D.; Dong, J.-F.; Qiu, Y.; Fu, L.; Feng, Y.; Hao, Y.; Wang, G.; Wang, J.; Liu, C.; Li, J.-F.; He, J.; Zhao, L.-D. Remarkable Electron and Phonon Band Structures Lead to a High Thermoelectric Performance ZT > 1 in Earth-Abundant and Eco-Friendly SnS Crystals. *J. Mater. Chem. A* **2018**, *6* 10048−10056.
40. Tan, Q.; Li, J.-F. Thermoelectric Properties of Sn-S Bulk Materials Prepared by Mechanical Alloying and Spark Plasma Sintering. *J. Electron. Mater.* **2014**, *43* 2435−2439.
41. Asfandiyar; Cai, B.; Zhao, L.-D.; Li, J.-F. High Thermoelectric Figure of Merit ZT > 1 in SnS Polycrystals. *J. Mater.* **2020**, *6* 77−85.
42. Wang, C.; Chen, Y.; Jiang, J.; Zhang, R.; Niu, Y.; Zhou, T.; Xia, J.; Tian, H.; Hu, J.; Yang, P. Improved Thermoelectric Properties of SnS Synthesized by Chemical Precipitation. *RSC Adv.* **2017**, *7* 16795−16800.
43. Prado-Gonjal, J.; Gainza, J.; Aguayo, I.; Durá, Ó. J.; Rodríguez-Pérez, S.; Serrano-Sánchez, F.; Nemes, N. M.; Fernández-Díaz, M. T.; Alonso, J. A.; Morán, E. High Thermoelectric Performance of Rapidly Microwave-Synthesized Sn1−δ_{1−\delta}1−δ S. *Mater. Adv.* **2020**, *1* 845−853.
44. Zhou, B.; Li, S.; Li, W.; Li, J.; Zhang, X.; Lin, S.; Chen, Z.; Pei, Y. Thermoelectric Properties of SnS with Na-Doping. *ACS Appl. Mater. Interfaces* **2017**, *9* 34033−34041.

45. Čermák, P.; Hejtmánek, J.; Plecháček, T.; Navrátil, J.; Kasparová, J.; Holý, V.; Zmrhalová, Z.; Jarošová, M.; Beneš, L.; Drašar, Č. Thermoelectric Properties and Stability of Tl-Doped SnS. *J. Alloys Compd.* **2019**, *811* 151902.
46. Niu, Y.; Chen, Y.; Jiang, J.; Pan, Y.; Yang, C.; Wang, C. Enhanced Thermoelectric Performance in Li Doped SnS via Carrier Concentration Optimization. *IOP Conf. Ser.: Mater. Sci. Eng.* **2020**, *738* 012016.
47. Zhang, H.; Liu, X.; Wang, J.; Zhang, B.; Chen, J.; Yang, L.; Wang, G.; Li, M.; Zheng, Y.; Zhou, X.; Han, G. Solution-Synthesized SnSe1−x_{1−x}1−xSx_xx: Dual-Functional Materials with Enhanced Electrochemical Storage and Thermoelectric Performance. *ACS Appl. Mater. Interfaces* **2021**, *13* 37201−37211.
48. Tan, Q.; Zhao, L.-D.; Li, J.-F.; Wu, C.-F.; Wei, T.-R.; Xing, Z.-B.; Kanatzidis, M. G. Thermoelectrics with Earth Abundant Elements: Low Thermal Conductivity and High Thermopower in Doped SnS. *J. Mater. Chem. A* **2014**, *2* 17302−17306.
49. He, W.; Wang, D.; Wu, H.; Xiao, Y.; Zhang, Y.; He, D.; Feng, Y.; Hao, Y.-J.; Dong, J.-F.; Chetty, R.; Hao, L.; Chen, D.; Qin, J.; Yang, Q.; Li, X.; Song, J.-M.; Zhu, Y.; Xu, W.; Niu, C.; Li, X.; Wang, G.; Liu, C.; Ohta, M.; Pennycook, S. J.; He, J.; Li, J.-F.; Zhao, L.-D. High Thermoelectric Performance in Low-Cost SnS0.91_{0.91}0.91 Se0.09_{0.09}0.09 Crystals. *Science* **2019**, *365* 1418−1424.
50. Hu, X.; He, W.; Wang, D.; Yuan, B.; Huang, Z.; Zhao, L.-D. Thermoelectric Transport Properties of N-Type Tin Sulfide. *Scr. Mater.* **2019**, *170* 99−105.
51. Zhi-Cheng, H.; Yao, Y.; Jun, P.; Jin-Feng, D.; Bo-Ping, Z.; Jing-Feng, L.; Peng-Peng, S. Preparation and Thermoelectric Property of N-Type SnS. *Inorg. Mater.* **2019**, *34* 321−327.
52. Dutta, M.; Sarkar, D.; Biswas, K. Intrinsically Ultralow Thermal Conductive Inorganic Solids for High Thermoelectric Performance. *Chem. Commun.* **2021**, *57* 4751−4767.

53. Maji, K.; Raveau, B.; Lemoine, P.; Boullay, P.; Acharyya, P.; Shen, X.; Renaud, A.; Pelletier, V.; Gautier, R.; Carnevali, V.; Fornari, M.; Zhang, B.; Zhou, X.; Lenoir, B.; Candolfi, C.; Guilmeau, E. Rattling of Three-Fold Coordinated Copper in Sulfides: A Blockade for Hole Carrier Delocalization but a Driving Force for Ultralow Thermal Conductivity. *J. Am. Chem. Soc.* **2024**, *146* 9741−9754.
54. Jobic, S.; Le Boterf, P.; Brec, R.; Ouvrard, G. Structural Determination and Magnetic Properties of a New Mixed Valence Tin Chromium Selenide: Cr2_22Sn3_33Se7_77. *J. Alloys Compd.* **1994**, *205* 139−145.
55. Rodriguez-Carvajal, J. Recent Advances in Magnetic Structure Determination by Neutron Powder Diffraction. *Phys. B* **1993**, *192* 55−69.
56. Roisnel, T.; Rodríguez-Carvajal, J. WinPLOTR: A Windows Tool for Powder Diffraction Pattern Analysis. *Mater. Sci. Forum* **2001**, *378−381* 118−123.
57. Thompson, P.; Cox, D. E.; Hastings, J. B. Rietveld Refinement of Debye−Scherrer Synchrotron X-Ray Data from Al2_22O3_33. *J. Appl. Crystallogr.* **1987**, *20* 79−83.
58. Vlassenbroeck, J.; Janssen, H.; Van Dooren, R. A Direct Chebyshev Approach with Practical Applicability in Optimal Control Problems. *IFAC Proc. Vol.* **1981**, *14 (2)* 417−422.
59. Dollase, W. A. Correction of Intensities for Preferred Orientation in Powder Diffractometry: Application of the March Model. *J. Appl. Crystallogr.* **1986**, *19* 267−272.
60. Coelho, A. A. TOPAS and TOPAS-Academic: an optimization program integrating computer algebra and crystallographic objects written in C++. *J. Appl. Crystallogr.* **2018**, *51* 210−218.
61. Prestipino, C. TEMpcPlot, 2023. https://github.com/Prestipino/TEMpcPlot.

62. Fei, Y.; Saxena, S. K. An Equation for the Heat Capacity of Solids. *Geochim. Cosmochim. Acta* **1987**, *51* 251−254.

63. Alleno, E.; Bérardan, D.; Byl, C.; Candolfi, C.; Daou, R.; Decourt, R.; Guilmeau, E.; Hébert, S.; Hejtmanek, J.; Lenoir, B.; Masschelein, P.; Ohorodnichuk, V.; Pollet, M.; Populoh, S.; Ravot, D.; Rouleau, O.; Soulier, M. Invited Article: A Round Robin Test of the Uncertainty on the Measurement of the Thermoelectric Dimensionless Figure of Merit of Co0.97_{0.97}0.97Ni0.03_{0.03}0.03Sb3_33. *Rev. Sci. Instrum.* **2015**, *86* 011301.

64. Blöchl, P. E. Projector Augmented-Wave Method. *Phys. Rev. B* **1994**, *50* 17953−17979.

65. Kresse, G.; Hafner, J. Ab Initio Molecular-Dynamics Simulation of the Liquid-Metal–Amorphous-Semiconductor Transition in Germanium. *Phys. Rev. B* **1994**, *49* 14251−14269.

66. Kresse, G.; Furthmüller, J. Efficient Iterative Schemes for Ab Initio Total-Energy Calculations Using a Plane-Wave Basis Set. *Phys. Rev. B* **1996**, *54* 11169−11186.

67. Perdew, J. P.; Ruzsinszky, A.; Csonka, G. I.; Vydrov, O. A.; Scuseria, G. E.; Constantin, L. A.; Zhou, X.; Burke, K. Restoring the Density-Gradient Expansion for Exchange in Solids and Surfaces. *Phys. Rev. Lett.* **2008**, *100* 136406.

68. Perdew, J. P.; Burke, K.; Ernzerhof, M. Generalized Gradient Approximation Made Simple. *Phys. Rev. Lett.* **1996**, *77* 3865−3868.

69. Wang, L.; Maxisch, T.; Ceder, G. Oxidation Energies of Transition Metal Oxides within the GGA+U Framework. *Phys. Rev. B* **2006**, *73* 195107.

70. Zunger, A.; Wei, S.-H.; Ferreira, L. G.; Bernard, J. E. Special Quasirandom Structures. *Phys. Rev. Lett.* **1990**, *65* 353−356.

71. Van De Walle, A.; Tiwary, P.; De Jong, M.; Olmsted, D. L.; Asta, M.; Dick, A.; Shin, D.; Wang, Y.; Chen, L. Q.; Liu, Z. K. Efficient Stochastic Generation of Special Quasirandom Structures. *Calphad* **2013**, *42* 13−18.

72. Hinuma, Y.; Pizzi, G.; Kumagai, Y.; Oba, F.; Tanaka, I. Band Structure Diagram Paths Based on Crystallography. *Comput. Mater. Sci.* **2017**, *128* 140−184.

73. Parlinski, K.; Li, Z. Q.; Kawazoe, Y. First-Principles Determination of the Soft Mode in Cubic ZrO2_22. *Phys. Rev. Lett.* **1997**, *78* 4063−4066.

74. Togo, A. First-Principles Phonon Calculations with Phonopy and Phono3py. *J. Phys. Soc. Jpn.* **2023**, *92* 012001.

75. Togo, A.; Chaput, L.; Tadano, T.; Tanaka, I. Implementation Strategies in Phonopy and Phono3py. *J. Phys.: Condens. Matter* **2023**, *35* 353001.

76. Pick, R. M.; Cohen, M. H.; Martin, R. M. Microscopic Theory of Force Constants in the Adiabatic Approximation. *Phys. Rev. B* **1970**, *1* 910−920.

77. Gonze, X.; Lee, C. Dynamical Matrices, Born Effective Charges, Dielectric Permittivity Tensors, and Interatomic Force Constants from Density-Functional Perturbation Theory. *Phys. Rev. B* **1997**, *55* 10355−10368.

78. Gajdoš, M.; Hummer, K.; Kresse, G.; Furthmüller, J.; Bechstedt, F. Linear Optical Properties in the Projector-Augmented Wave Methodology. *Phys. Rev. B* **2006**, *73* 045112.

79. Yamada, T.; Yoshiya, M.; Kanno, M.; Takatsu, H.; Ikeda, T.; Nagai, H.; Yamane, H.; Kageyama, H. Correlated Rattling of Sodium-Chains Suppressing Thermal Conduction in Thermoelectric Stannides. *Adv. Mater.* **2023**, *35* 2207646.

80. Corps, J. Structural and Physical Properties of Low-Dimensional Chalcogenides. Thesis, Heriot-Watt University, 2014. https://www.ros.hw.ac.uk/handle/10399/2786.

81. Adenis, C.; Olivier-Fourcade, J.; Jumas, J.-C.; Philippot, E. Etudes Sur Le Système Ternaire Sn-In-S. Analyses Thermique Differentielle et Radiocristallographique Du Pseudobinaire SnS- In2S3. Croissance En Phase Vapeur et Caracterisation de Composeś a Valences Mixtes de l'etain. *J. Solid State Chem*. 1986, 65, 251−259.
82. Adenis, C.; Olivier-Fourcade, J.; Jumas, J.-C.; Philippot, E. Etude Structurale de In2Sn3S7Par Spectrométrie Mössbauer de 1199Sn et Diffraction Des Rayons X. *Rev. Chim. Miner.* **1986**, *23* 735−745.
83. Sleight, A. W.; Frederick, C. G. Preparation of Ferrimagnetic SnCr2S4*Mater. Res. Bull.* **1973**, *8* 105−107.
84. Landa-Cánovas, A.; Gómez-Herrero, A.; Carlos Otero-Díaz, L. Electron Microscopy Study of Incommensurate Modulated Structures in Misfit Ternary Chalcogenides. *Micron* **2001**, *32* 481−495.
85. Jellinek, F. The Structures of the Chromium Sulphides. *Acta Crystallogr.* **1957**, *10* 620−628.
86. Wiedemeier, H.; Georg, H.; Schnering, G. von. Refinement of the Structures of GeS, GeSe, SnS and SnSe. *Z. Kristallogr.* **1978**, *148* 295−304.
87. Jobic, S.; Bodenan, F.; Ouvrard, G.; Elkaim, E.; Lauriat, J. P. Structural Determination and Magnetic Properties of a New Orthorhombic Chromium Seleno Stannate, Cr2Sn3Se7. *J. Solid State Chem.* **1995**, *115* 165−173.
88. Brown, I. D. Recent Developments in the Methods and Applications of the Bond Valence Model. *Chem. Rev.* **2009**, *109* 6858−6919.
89. Adenis, C.; Olivier-Fourcade, J.; Jumas, J.-C.; Philippot, E. Structural Study of In6Sn8S19a Mixed Valence Tin Phase in the Ternary System In-Sn-S. *Eur. J. Solid State Inorg. Chem.* **1988**, *25* 413−423.

90. Lefebvre, I.; Lannoo, M.; Olivier-Fourcade, J.; Jumas, J. C. Tin Oxidation Number and the Electronic Structure of SnS-In2_22Sn3_33-SnS2_22 Systems. *Phys. Rev. B* **1991**, *44* 1004−1012.

91. Shastri, S. S.; Pandey, S. K. Thermoelectric Properties, Efficiency and Thermal Expansion of ZrNiSn Half-Heusler by First-Principles Calculations. *J. Phys.: Condens. Matter* **2020**, *32* 355705.

92. Dudnik, E. M.; Oganesyan, V. Kh. Thermal Expansion of Some Sulfides of the Transition Metals. *Powder Metall. Met. Ceram.* **1966**, *5* 125−127.

93. Chetty, R.; Kikuchi, Y.; Bouyrie, Y.; Jood, P.; Yamamoto, A.; Suekuni, K.; Ohta, M. Power Generation from the Cu26_{26}26Nb2_22Ge6_66S32_{32}32-Based Single Thermoelectric Element with Au Diffusion Barrier. *J. Mater. Chem. C* **2019**, *7* 5184−5192.

94. Lemoine, P.; Pavan Kumar, V.; Guélou, G.; Nassif, V.; Raveau, B.; Guilmeau, E. Thermal Stability of the Crystal Structure and Electronic Properties of the High Power Factor Thermoelectric Colusite Cu26_{26}26Cr2_22Ge6_66S32_{32}32. *Chem. Mater.* **2020**, *32* 830−840.

95. Wiedemeier, H.; Csillag, F. J. The Thermal Expansion and High Temperature Transformation of SnS and SnSe. *Z. Kristallogr.* **1979**, *149* 17−30.

96. Lippens, P. E. Interpretation of the 119^\text{119}119Sn Mössbauer Isomer Shifts in Complex Tin Chalcogenides. *Phys. Rev. B* **1999**, *60* 4576−4586.

97. Di Benedetto, F.; Bernardini, G. P.; Borrini, D.; Lottermoser, W.; Tippelt, G.; Amthauer, G. 57^\text{57}57Fe− and 119^\text{119}119Sn− Mössbauer Study on Stannite (Cu2_22FeSnS4_44)-Kesterite (Cu2_22ZnSnS4_44) Solid Solution. *Phys. Chem. Miner.* **2005**, *31* 683−690.

98. Elidrissi-Moubtassim, M. L.; Olivier-Fourcade, J.; Jumas, J.-C.; Senegas, J. Etude de l'insertion de Lithium Dans In16Sn4S32Par RMN (7Li) et Spectrométrie Mössbauer (119Sn). *J. Solid State Chem.* **1990**, *87* 1−9.

99. de Kergommeaux, A.; Faure-Vincent, J.; Pron, A.; de Bettignies, R.; Malaman, B.; Reiss, P. Surface Oxidation of Tin Chalcogenide Nanocrystals Revealed by ^{119}Sn−Mössbauer Spectroscopy. *J. Am. Chem. Soc.* **2012**, *134* 11659−11666.

100. Morrish, A. H. *The Physical Principles of Magnetism*; Wiley-IEEE, 2001.

101. Yue, G. H.; Peng, D. L.; Yan, P. X.; Wang, L. S.; Wang, W.; Luo, X. H. Structure and Optical Properties of SnS Thin Film Prepared by Pulse Electrodeposition. *J. Alloys Compd.* **2009**, *468* 254−257.

102. Gebredingle, Y.; Joe, M.; Lee, C. Cr2S3 Bipolar Semi- conducting Fully Compensated Ferrimagnet. *Phys. Rev. Mater.* **2022**, *6* (5), 054405.

103. Xie, L.; Wang, J.; Li, J.; Li, C.; Zhang, Y.; Zhu, B.; Guo, Y.; Wang, Z.; Zhang, K. An Atomically Thin Air-Stable Narrow-Gap Semiconductor Cr2S3 for Broadband Photodetection with High Responsivity. *Adv. Electron. Mater.* **2021**, *7* (7), 2000962.

104. Tang, W.; Sanville, E.; Henkelman, G. A Grid-Based Bader Analysis Algorithm without Lattice Bias. *J. Phys.: Condens. Matter* **2009**, *21* (8), 084204.

105. Silvi, B.; Savin, A. Classification of Chemical Bonds Based on Topological Analysis of Electron Localization Functions. *Nature* **1994**, *371* (6499), 683−686.

106. Dimitrov, I. K.; Manley, M. E.; Shapiro, S. M.; Yang, J.; Zhang, W.; Chen, L. D.; Jie, Q.; Ehlers, G.; Podlesnyak, A.; Camacho, J.; Li, Q. Einstein Modes in the Phonon Density of States of the Single-Filled Skutterudite $Yb_{0.2}Co_4Sb_{12}$. *Phys. Rev. B* **2010**, *82* (17), 174301.

107. Takabatake, T.; Suekuni, K.; Nakayama, T.; Kaneshita, E. Phonon-Glass Electron-Crystal Thermoelectric Clathrates: Experiments and Theory. *Rev. Mod. Phys.* **2014**, *86* (2), 669−716.

108. Grüneisen, E. Theorie Des Festen Zustandes Einatomiger Elemente. *Ann. Phys.* **1912**, *344* (12), 257−306.

109. Acharyya, P.; Pal, K.; Zhang, B.; Barbier, T.; Prestipino, C.; Boullay, P.; Raveau, B.; Lemoine, P.; Malaman, B.; Shen, X.; Renaud, A.; Uberuaga, B.; Candolfi, C.; Zhou, X.; Guilmeau, E. Structure Low Dimensionality and Lone Pair Stereochemical Activity, the Key to Low Thermal Conductivity in Pb-Sn-S System. *J. Am. Chem. Soc.* **2024**, *146* (19), 13477−13487.

110. Saito, W.; Hayashi, K.; Nagai, H.; Miyazaki, Y. Preparation and Thermoelectric Properties of Mixed Valence Compound Sn_2S_3. *Jpn. J. Appl. Phys.* **2017**, *56* (6), 061201.

111. Chang, Y.; Ruan, M.; Li, F.; Zheng, Z.; Chen, Y.; Ge, Z.; Fan, P. Synthesis Process and Thermoelectric Properties of the Layered Crystal Structure SnS_2. *J. Mater. Sci.: Mater. Electron.* **2020**, *31* (7), 5425−5433.

112. Skelton, J. M.; Burton, L. A.; Jackson, A. J.; Oba, F.; Parker, S. C.; Walsh, A. Lattice Dynamics of the Tin Sulphides SnS_2, SnS and Sn_2S_3: Vibrational Spectra and Thermal Transport. *Phys. Chem. Chem. Phys.* **2017**, *19* (19), 12452−12465.